ABSTRACT

Title of Document:	FUNCTIONALLY COATED FACETED ALUMINUM NANOCRYSTALS: AEROSOL SYNTHESIS AND REACTIVITY
	Daniel A. Kaplowitz, Doctorate of Philosophy, 2013
Directed By:	Professor Michael R. Zachariah Department of Mechanical Engineering and Department of Chemistry & Biochemistry

The demand for large scale manufacture of nanoaluminum for use in propellant applications has motivated research into development of an aerosol production scheme. In addition, the reactive nature of aluminum in the presence of oxygen has inspired investigation into functionally coating bare nanoaluminum prior to exposure to the atmosphere. Faceted aluminum crystals are fabricated in the aerosol phase via thermal pyrolysis of triisobutylaluminum, a low temperature gas-phase synthesis route, and combustion tests of oxygen passivated product in thermite combination show an increase in energy release compared to commercial nanoaluminum. Three different coatings on this bare nanoaluminum are developed: a decoration of Ni/Ni_2O_3 particles by thermal decomposition of $Ni(CO)_4$, a homogeneous layer of Fe_3O_4 by thermal decomposition of $Fe(CO)_5$, and a monolayer of perfluoropentanoic acid via bridge bonding between aluminum and carboxylate groups. X-ray photoelectron spectroscopy analysis indicates that the metal oxide coatings have facilitated formation of an expanded aluminum oxide

layer during an air bleed, but perfluoropentanoic acid has successfully passivated aluminum. The protection from significant oxide formation for the perfluoropentanoic acid coating is evident in a 16% increase in active fuel content by thermogravimetric analysis compared to the untreated case. Subsequent temperature jump fine wire combustion tests show decreased ignition temperatures for all three coatings. Combustion chamber tests in thermite combinations display poor pressure output for the Ni/Ni_2O_3 coated case, but reasonable response for the Fe_3O_4 product. Flame ignition of perfluoropentanoic acid coated product is shown to produce AlF_3 by chemical analysis of char, indicating the passivation coating also functions in direct oxidizer delivery.

LAY ABSTRACT

A new method is developed for low cost manufacturing of small “nano” aluminum particles needed for rocket fuel applications. The aluminum particles are then mixed with copper oxide, which serves as an oxygen source for the aluminum fuel. When evaluated for its combustion performance, the new aluminum product gives a much better energy release compared to commercial aluminum particles, a key aspect for use as rocket fuel.

Such small particles are too reactive to be used in their newly generated form, so a thin protective coating is needed. Three different coatings around the aluminum particles are formed to protect the aluminum and improve its reactivity. I develop a coating approach that directly combines with the aluminum particle manufacture in a continuous process. Two different metal oxides and a fluorocarbon are studied separately as coating materials. Analysis of the coated particles shows that the metal oxide layers cannot protect aluminum while the fluorocarbon layer is successful in protection. Burn tests for these products display earlier ignition for all three coated aluminum samples, a valuable trait for use in rocket fuel. Further tests show that the thin metal oxide coating allows for a proper energy release when burned, but the thick metal oxide coating blocks this release. For the fluorocarbon coated sample, a desired reaction between aluminum and fluorine is confirmed. Thus this fluorocarbon coating approach accomplishes the main goal of forming a protective layer that can also improve reactivity.

FUNCTIONALLY COATED FACETED ALUMINUM NANOCRYSTALS: AEROSOL SYNTHESIS AND REACTIVITY

By

Daniel A. Kaplowitz

Thesis submitted to the Faculty of the Graduate School of the
University of Maryland, College Park in partial fulfillment
of the requirements for the degree of
Doctorate of Philosophy
2013

Advisory Committee:

Professor Michael R. Zachariah, Committee Chair
Professor Panagiotis Dimitrakopoulos
Professor Sheryl Ehrman
Professor Srinivasa Raghavan
Professor Philip DeShong, Dean's Representative

Acknowledgment

I would like to sincerely thank my family and friends for their continued support and guidance throughout my graduate and undergraduate education and research. Many thanks to fellow group members for their assistance in experimentation and analysis, and further gratitude to my advisor for lending his knowledge and expertise in the aerosol and energetics fields.

Table of Contents

List of Tables

List of Figures

List of Abbreviations

CAA ..... Commercial Air Atomization
CIGA ..... Commercial Inert Gas Atomization
CPC ..... Condensation Particle Counter
CVC ..... Chemical Vapor Condensation
CVD ..... Chemical Vapor Deposition
DMA ..... Differential Mobility Analyzer
EDS ..... Energy Dispersive X-ray Spectroscopy
FC ..... Fluorocarbon
FTIR ..... Fourier Transform Infrared Spectroscopy
FWHM ..... Full Width Half Max
GARS ..... Gas Atomization Reaction Synthesis
GEM ..... Gas Evaporation Method
HRTEM ..... High Resolution Transmission Electron Microscopy
MCT ..... Mercury Cadmium Telluride
MIC ..... Metastable Intermolecular Composite
PFPA ..... Perfluoropentanoic Acid
SMPS ..... Scanning Mobility Particle Sizer
TEM ..... Transmission Electron Microscopy
TGA ..... Thermogravimetric Analysis
TibAl ..... Triisobutylaluminum
T-jump ..... Temperature Jump
XPS ..... X-ray Photoelectron Spectroscopy

Chapter 1: Introduction and Background

1.1 Metal Oxidizer Combinations

The high energy content of metal/oxidizer combinations compared to CHNO based materials has motivated considerable investigation into energetic applications requiring rapid energy release [1,2]. Tailored preparation methods may allow their replacement of conventional energetic materials for certain military and civilian applications including propellants, explosives, and pyrotechnics, as detailed by Piercey and Klapötke in their review of nanoscale aluminum thermite reactions [3]. The reaction for these metal/oxidizer combinations is relatively simple but can be very effective.

$$M_1O(s) + M_2(s) \rightarrow M_1(s) + M_2O(s) + \Delta H \quad (1)$$

As shown in Equation 1, M_1O performs as the metal oxidizer and M_2 the fuel. Maximizing the exotherm from this reaction is accomplished by selecting appropriate metallic components. Employing a fuel with high energy density and reactive nature will result in the high yield and rapid oxidation required for propellant applications.

Reactive metals can have an extremely high energy density, as seen in Figure 1.1, but performance is hindered by diffusion limited kinetics between oxidizer and metal. This is partially mitigated by going to smaller particle sizes in order to increase the surface to volume ratio of the aluminum particle. Decreasing particle size to the nanometer range yields a substantial increase in surface area compared to particles of micron size and can substantially increase reaction rate.

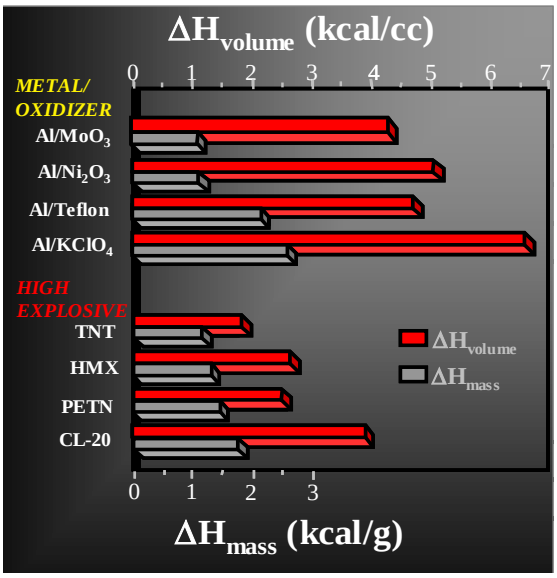

Figure 1.1: Energy content comparisons for metal oxidizer combinations and CHNO based materials [4,5].

Almost all reactive metals become pyrophoric for particles under 100 nm. Proper mixing of reactive metal nano-thermite combinations results in a metastable intermolecular composite (MIC) that can bypass mass diffusion restrictions and allow for kinetically controlled highly customizable reactions. A representation of such a mixture is shown in Figure 1.2 with aluminum as the fuel.

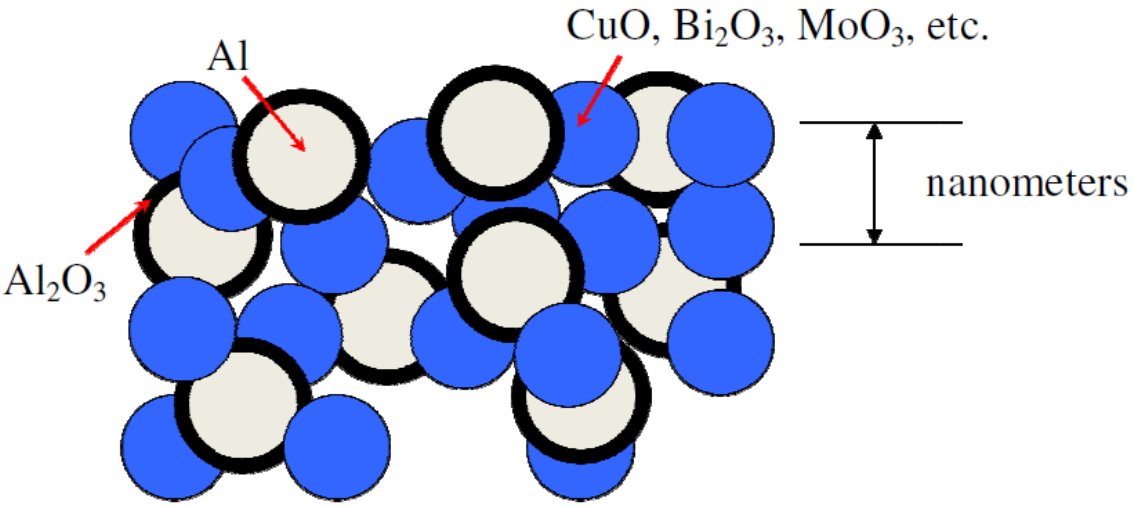

Figure 1.2: Simple schematic of a metastable intermolecular composite with nanosized aluminum fuel.

1.2 Nanoaluminum

For energetic formulations in the nanoregime, aluminum is the leading fuel component due to its ready availability, low materials cost, and high heat of reaction to the oxide [6-8]. While many different nanoscale oxidizers are employed, aluminum is a main focus. There is currently a large demand for nanoaluminum for propellant mixture applications, yet there are no large scale manufacturing processes. Smaller scale production exists, but these routes yield very expensive nanoaluminum on the scale of $1000 per kilogram.

A major concern with production and use of nanoaluminum, however, is the native oxide that naturally forms when any bare aluminum is exposed to air. For micron size aluminum particles, this 3-5 nm oxide layer accounts for only a small fraction of the particle mass. For nanosized aluminum, this oxide coating can represent a large fraction of the particle's mass. A 50 nm particle with a 5 nm alumina shell will contain 58% of the particle's total mass as aluminum oxide, leaving a much smaller amount of material available for an energetic process. The other concern with this alumina layer is its significant impedance to reaction due to its poor reactivity and high melting point of 2072 °C compared to aluminum's 660 °C. For further reaction between aluminum and oxygen, the core material must either escape the shell or oxidizer must diffuse through [9,10]. The focus in this work is an approach to form a different layer that will enhance aluminum transport and reactivity.

1.3 Coating Nanoaluminum

Developing a coating before oxidation can occur is the most common technique to prevent surface oxidation of aluminum [11-15]. Such a passivation layer can be used for

storage and prevent significant loss of fuel. A nonpyrophoric coated nanoaluminum, for example, was prepared by Hammertroem *et al.* by polymerizing epoxides on the particle surface in solution [11]. This chemical reaction with the exposed aluminum atoms keeps them occupied and prevents reaction with ambient oxygen. The drawback with such techniques, however, is the unproductive mass attributed to coating material in the product. Loss of active aluminum is prevented, but the product can still have significant content attributed the polymerized coating unlikely to contribute to an energetic event. Development of a passivation coating that can be removed before combustion could alleviate this issue, but this could prove difficult with a chemically bound coating layer.

A more valuable approach could be to develop a functional energetic material coating that can directly react with the aluminum core during combustion. This functionalized layer on bare aluminum would not only prevent the oxide shell from forming, but would also affect agglomeration during processing and alter the energy release mechanisms during combustion. If an oxidizer is attached directly to the aluminum surface while preventing a spontaneous run-away reaction, the resulting structure will have higher energy content with the potential of favorably altered kinetics.

1.4 Metal Coating

Metals can be used for coating bare nanoaluminum to improve energetic function. Iron has successfully been coated on the surface of micron sized aluminum particles by chemical precipitation methods. These particles have shown decreased agglomeration during combustion, thus increasing their efficiency. The premise behind this phenomenon, demonstrated by Breiter *et al.*, is that increasing the surface metal melting temperature above the combustion temperature yields a significant decrease in agglomeration during a

combustion event [16]. Since Fe has a much higher melting temperature than Al, 1538 °C compared to 660 °C, a coating allows for less agglomeration when burning and therefore a more efficient material. Burn tube experiments with this product showed a significant enhancement in flame speed compared to untreated aluminum. Metal coated aluminum particles have also exhibited decreased critical ignition temperatures, theorized by Shafirovic *et al.* to be due to exothermic alloying reactions [17]. Andrzejak *et al.* found evidence of this Al-Fe alloying for millimeter particle sized iron coated aluminum that resulted in significantly lowered ignition temperatures during laser combustion experiments [18].

A similar exothermic alloying reaction between Al and Ni has shown potential for yielding decreased critical ignition temperature [17]. This alloying reaction releases a significant amount of energy and has been theorized as a useful material for applications lacking oxygen in the atmosphere. Henz *et al.* [19] have developed molecular dynamic simulations of the alloying reaction between Al and Ni particles to explore the reaction mechanism and effect of particle size. This was accomplished for both separate Al and Ni particles as well as for Al coated with Ni. Developing a new approach for producing such a coating could prove to be valuable.

1.4.1 Oxidation of Metal Coating Layers

For a nanoscale coating, however, it is unlikely for a 1-3 nm layer of reactive metal to remain in the elemental state upon exposure to air due to the highly pyrophoric nature. Most likely a thin coating of iron, for example, would react with oxygen, resulting in an iron oxide layer on the aluminum surface. This outcome does not necessarily ruin the functionality of such a coating layer. Work by La *et al.* has shown that for appropriate

powder mixing stoichiometries, iron oxide and aluminum can react to form Fe_3Al according to the reaction shown in Equation 2 [20].

$$3Fe_2O_3 + 8Al \rightarrow 2Fe_3Al + 3Al_2O_3 \quad \Delta H^o = -2550\,\text{kJ} \tag{2}$$

The energy released from this exothermic reaction could alter combustion characteristics in a thermite reaction with a thin layer of iron oxide coated on the aluminum surface. As nickel is less pyrophoric than iron, there is a higher likelihood of retaining pure nickel metal on the particle surface. A percentage of the nickel will most likely oxidize once in contact with oxygen, but retaining some pure metal will promote the exothermic Al-Ni reaction during combustion.

1.5 Organic Coating

Coating with organic layers presents more opportunity to chemically bond with aluminum to passivate. Jouet *et al.* successfully prevented oxidation of nanoaluminum by forming a monolayer of a perfluorotetradecanoic acid ($C_{14}HF_{27}O_2$) on the particle surface in solution, thus functionalizing the surface to enhance reactivity [12]. Subsequent shock reactivity testing of the product combined with organic high explosives shows a significant enhancement compared to conventional Al, and laser ignition experiments show fast reaction capacities for the passivated product [13]. Horn *et al.* prepared similar perfluorocarboxylic acid coatings on nanoaluminum particles that had already formed an oxide layer [21]. This product in thermite combinations demonstrated via flame tests that even without passivation, energetic improvement can still be achieved from direct oxidizer delivery in a nanoparticle coating [22].

Fluorination of aluminum to produce AlF_3 can produce a significant increase in energy release, 3.18 kJ per gram of aluminum, compared to formation of Al_2O_3 which

releases 1.77 kJ/g [21]. The stoichiometric exothermic reaction of aluminum with fluorocarbon will produce AlF_3 and carbon according to the reaction shown in Equation 3 [23].

$$2Al + 3(-CF_2-)_n \rightarrow 3C + 2AlF_3 \quad \Delta H^0 = -591.98\,\text{kJ} \tag{3}$$

Teflon has been heavily focused on for studies involving fluorination of aluminum. Watson *et al.* examined combustion reactions for aluminum/Teflon compared to aluminum/MoO_3 combinations for closed and open configurations, concluding that for closed system combustion, fluorine oxidizing combinations can yield increased heat of combustion and gas generation compared to the metal oxide [24]. For open system combustion, however, they found that the higher gas generation can hinder the reaction due to loss of the liberated gas.

Further investigation into the mechanism for interaction between fluorine and aluminum was undertaken by Pantoya *et al.*, probing a pre-ignition reaction between aluminum oxide and fluorine [25]. Differential scanning calorimetry-thermogravimetric analysis experiments for aluminum oxide nanoparticles combined with Teflon showed a significant exotherm starting at 400 °C indicating fluorination of aluminum oxide. This suggests that not only can fluorocarbon combinations with aluminum metal powder provide increased energy release, an early fluorine reaction with an aluminum oxide layer could change the combustion reaction mechanism and avoid issues with the poor reactivity and high melting point of the aluminum oxide shell.

1.6 Aerosol Approach

Aerosol processes are the production method of choice for most industrial nanopowder generation processes. The reason for the abundant use of aerosol

manufacturing lies in its inherent continuous flow process. Aerosol can be generated in a constant stream and combined with any other process to yield a desirable product, all accomplished at a low cost. Liquid methods, though proven effective, are often batch processes where long reaction times, recycling solvent, and cleaning costs quickly add up as production scale increases. Gas phase systems are also generally simpler, allowing for easy scale up from the research phase to large scale. In the research stage, as well, aerosol systems are generally the most useful approach for studying particles, allowing for a high level of control for a small amount of material.

Aerosol dynamics covers a broad spectrum of applications, from the growth of carbon nanotubes to the development of nanoparticles for drug delivery. A vast amount of theoretical and technical research has been accomplished in this area and can be applied to this research [26]. The flow of particles, the use of an aerosol reactor, and product characterization methods are just a few of the topics intensely studied by the aerosol community and applied in this research.

1.7 Aerosol Characterization

In my experimentation, I use two pieces of equipment for the aerosol studies; a differential mobility analyzer (DMA) and a condensation particle counter (CPC). When the DMA and CPC are combined, one can readily obtain a size distribution measurement of particle product. This information is critical for determining the effect of process variables and comparing results.

The DMA is a tool used for particle size selection for aerosols, allowing only particles of tuned size to exit. The approach for this separation is a balance of electrostatic and Stokes' drag forces on a given particle. Polydisperse aerosol is sent between two

concentric metal cylinders, and a tunable electric field is applied. As shown in Figure 1.3, charged particles enter the chamber, combine with a sheath flow, and are subjected to the electric field. As particles are pulled in one direction by the electric field, Stokes' drag forces resist the flow. As this drag force is dependent on the surface area of the particle, selection of a particular electric potential across the cylinders to balance the drag force permits only particles of one size to pass through the monodisperse aerosol exit slit at the bottom of the chamber. Particles of undesired size are either impacted on the walls of the chamber or are exhausted though a separate exit.

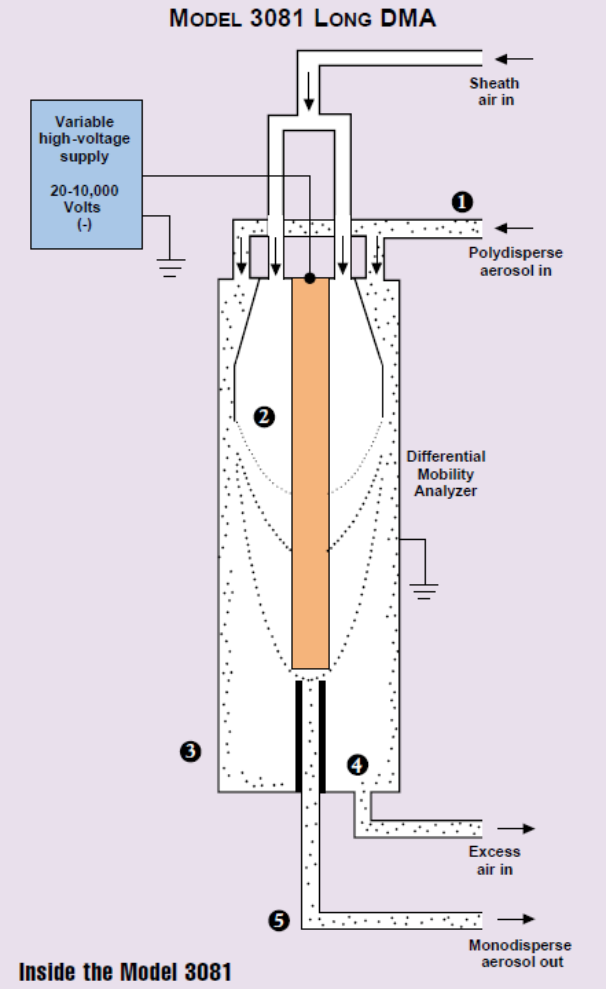

Figure 1.3: Model 3081 Long DMA [27].

Stages in Figure 1.3 are labeled to show each important step in the size selection process. Polydisperse charged aerosol flow is sent into the chamber in region (1). Next, charged particles are attracted to either the center rod (2) or the wall (3). Excess particles exit the exhaust in region (4), and finally the particles of the selected size based on tuned voltage exit the small slit in region (5).

Thus, the flow exiting the DMA is monodisperse aerosol that can be sent to other equipment for further characterization. It should be noted that the calculations used to associate the measured surface area of a particle with an electrical mobility are for spherical particles. Since many particles sent through the DMA can be nonspherical or agglomerated masses, there is an error associated with this measurement. Furthermore, Brownian motion must be accommodated in drag force calculations for nanosized particles. In *Smoke, Dust, and Haze*, Friedlander shows how to account for this adjustment [26].

The other main tool used in aerosol characterization is the condensation particle counter, a device that measures the concentration of particles in a gas. Since nanoparticles are too small to conduct single particle light scattering for counting purposes, the particles are grown in a supersaturated butanol vapor to ~10 μm so that individual light scattering can be achieved. The CPC can be used on its own to measure the concentration of a polydisperse aerosol, but it can become a more powerful tool when combined with the DMA to measure the concentration of size selected particles.

The scanning mobility particle sizer (SMPS) system consists of the DMA working in conjunction with the CPC in such a way that a size distribution is obtained. The DMA has a function that allows it to scan through the entire range of voltages or particle sizes. The outlet from the DMA is connected to the CPC, and by taking a count when the DMA

stops at each voltage, a distribution of particle concentration is constructed for the polydisperse aerosol.

These devices and systems allow for accurate measurement of an aerosol product, a valuable tool for designing and altering an aerosol system in the experimental phase. An unreacted sample can be characterized before and after oxidation. Two aerosol systems can be combined and interpreted. Experimental size distributions can be used to evaluate theoretical models for aerosol production. If the two do not match, process or modeling issues can be identified. As the focus is on developing functional layers on an existing aluminum aerosol, accurate production measurements of core and coating material are a necessity. As a result, these means are used repeatedly in this work to produce nanoaluminum and develop functional coatings.

Chapter 2: Bare Nanoaluminum Synthesis

2.1 Literature Review

In order to synthesize nanoaluminum in an oxygen free environment for subsequent coating, an appropriate fabrication scheme had to be selected. As previously described, further experimentation into low cost production of nanosized aluminum is necessary to find larger scale production techniques. An aerosol process allows continuous production with simple design and thus relatively easy scale-up compared to solution based processes that can have long reaction times and excessive solvent requirements leading to high manufacturing costs. If a production scheme can yield aluminum in an aerosol flow avoiding immediate formation of an oxide shell, further manipulation via coating could alleviate major industrial concerns with active fuel loss and reactivity limitations.

To choose an appropriate nanoaluminum approach, a survey of current processes was necessary. Park *et al.* [28] explored several methods for production of nanoaluminum in aerosol form. Al was evaporated from solid pellets via a DC-arc discharge method that created nanoparticles upon quenching with argon gas. A second method used laser ablation to create a local microplasma on aluminum pellets that again yielded nanoparticles after an argon quench. Exploding wire has also been extensively employed for gas phase production of nanoaluminum [29-32]. This technique uses a high density current pulsed through an Al wire to create a microplasma which yields ultra-fine aluminum after a quench. Sindhu *et al.* [33] combined experimental and modeling studies to fully characterize the explosive Al wire process. Anderson *et al.* [34] investigated gas atomization reaction synthesis (GARS) for Al, a powder production technique where the molten metal is atomized in an environment of ultra-high purity inert gas. This allows for

growth of an extremely thin oxide coating on the Al product compared to particles made from commercial air atomization (CAA) or commercial inert gas atomization (CIGA).

These methods, while seeming to be very different, all essentially involve a very high temperature evaporation of elemental aluminum followed by a rapid quench. Not surprising, then, is that these methods tend to produce similar types of polycrystalline particles with primary particle sizes less than ~50 nm that are highly aggregated. Low temperature routes have been successfully developed for decomposition of aluminum compounds in solution. Jouet *et al.* [12] catalytically decomposed in liquid phase $H_3Al{\cdot}NMe_3$ in organic solvents under inert gas. The bare nanoaluminum product was then surface passivated with a perfluoroalkyl carboxylic acid monolayer to prevent oxidation. Other successful liquid phase production methods include reaction of $LiAlH_4$ with $AlCl_3$ [35], hydrogenolysis of $(AlCp^*)_4$ [36], and thermal decomposition of Alane N,N-Dimethylethylamine [37].

A low temperature gas phase route is explored, through the use of a metal organic precursor that has a decomposition temperature below the melting point of aluminum, as a means to carefully control the nucleation and growth of nanoaluminum. This work will demonstrate that thermal decomposition of triisobutylaluminum (TibAl), under the appropriate time/temperature histories, can generate highly faceted nanocrystals of aluminum. These materials are then tested for their reactivity relative to conventional nanoaluminum.

The choice of precursor was specifically targeted to create vapor phase reaction products containing aluminum or elemental aluminum below the melting point of aluminum (660 °C) so that particle growth occurs at or near a solid like state. TiBAl was

chosen as a precursor due to its relatively low decomposition temperatures. Previous work in chemical vapor deposition (CVD) has shown that TiBAl can be decomposed at temperatures in the range of 250 °C to deposit thin films of aluminum with little carbon contamination [38-40]. This low decomposition temperature and its relatively high vapor pressure are both highly desirable properties for scale up of aluminum production in large quantities. The mechanism of TiBAl decomposition also has been explored in previous CVD work and involves deposition on the substrate, β-hydride elimination, and finally liberation of isobutylene and hydrogen, leaving elemental aluminum on the substrate. Due to the substrate's role in the β-hydride elimination, it is not clear if the mechanism and energetics for gas-phase aluminum production will be comparable. However, previous efforts with triethylaluminum as the precursor yielded incomplete decomposition, suggesting the isobutylene is a better leaving group than ethylene and thus further supporting the β-hydride elimination mechanism.

2.2 Experimental Setup

2.2.1 Aluminum Synthesis

The synthesis scheme involves a continuous flow aerosol reactor. The precursor delivery system consists of a heated stainless steel bubbler filled with the liquid TibAl precursor, through which a mass-flow metered ultra-high purity argon flow is bubbled at 3000 sccm. Temperature control is monitored with a thermocouple placed in a thermowell built into the bubbler. Assuming complete vapor saturation of the argon flow based on the known vapor pressure of TibAl, the expected aluminum production rates are shown in Table I based on typical operating conditions.

Table I. Theoretical Production for TibAl Vaporization and Decomposition.

Temp (°C)	VP TibAl (Pa)	TibAl (g/hr)	Al (g/hr)
50	122.6	1.63	0.222
60	281.3	3.63	0.493
70	439.9	5.51	0.749

Though increasing bubbler temperature by only 10 degrees yields a substantial increase in theoretical production rate, temperatures were not raised above 70 °C to avoid any significant decomposition of the precursor [41].

Since both the precursor and the aluminum nanoparticle product are highly air and water sensitive, the flow train was valved so as to allow extensive flushing with argon prior to and after each experiment to ensure complete oxygen removal from the system. The stainless steel 0.25 inch piping at the bubbler outlet leading to the furnace was heat jacketed and kept at the same temperature as the bubbler to prevent condensation of the precursor prior to the flow reactor. The synthesis system consists of a one inch diameter quartz tube heated within a 15.5 inch tube furnace. Experiments with a flow rate of 3000 sccm through the reactor yield a residence time of 3.96 s. A schematic for the experimental setup is shown in Figure 2.1. Particles exiting the reactor were collected on Sterlitech 47 mm polypropylene membrane filters with a pore size of 200 nm in a Millipore stainless steel filter holder. Since the particles produced are oxygen free, they were highly reactive. To harvest the particles on the filters for characterization, a lean air/argon mix is carefully bled in so as to create an oxide passivation shell on the particles. Product aerosol could also be electrostatically deposited onto transmission electron microscopy (TEM) grids using a TSI Aerosol Sampler, or sent to the SMPS system for size distribution measurements.

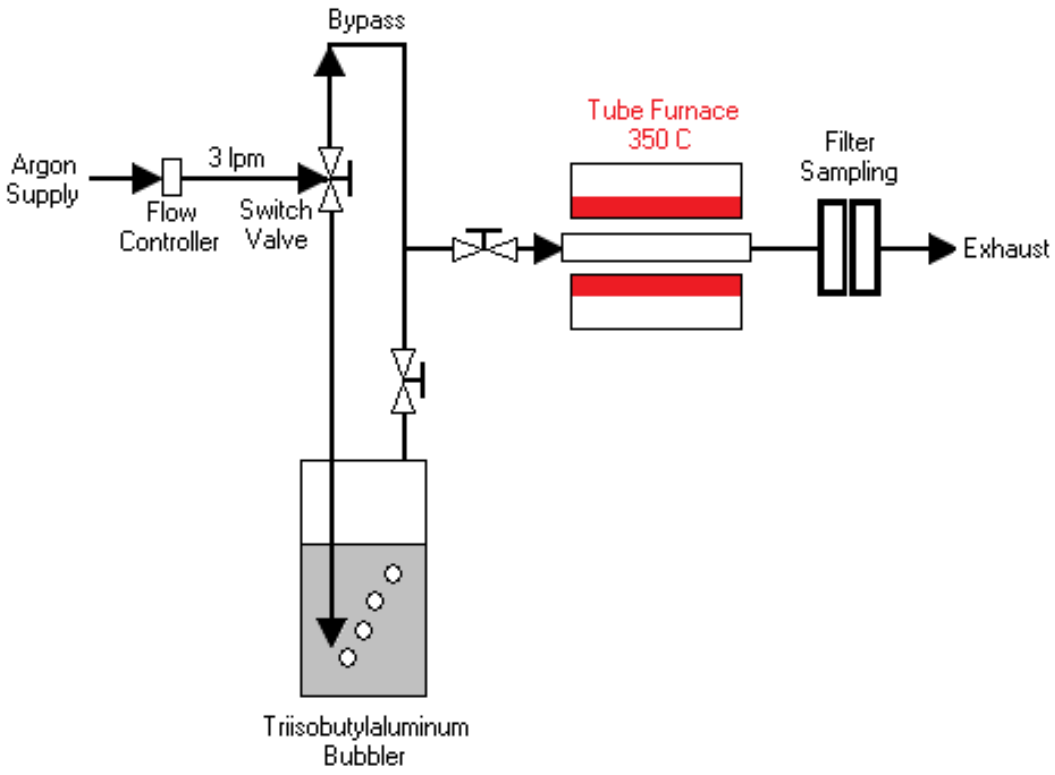

Figure 2.1: Schematic of aerosol synthesis system of aluminum nanocrystals via thermal pyrolysis of triisobutylaluminum.

2.2.2 Product Evaluation Apparatus

– High Resolution Transmission Electron Microscopy (HRTEM): the collected sample was deposited on carbon film 200 mesh copper grids from Electron Microscopy Sciences for high resolution TEM imaging (JEOL JEM 2100FE-TEM) with a focus on the particle edge. The system can be coupled with energy dispersive X-ray spectroscopy (EDS) for elemental analysis.

– X-ray Photoelectron Spectroscopy (XPS) Characterization: samples are inspected with a Kratos AXIS 165 spectrometer operated in hybrid mode and excited with monochromated aluminum X-rays at 280 W in an ultrahigh vacuum chamber with a base pressure $\leq 5 \cdot 10^{-8}$ torr. Charge neutralization is required to minimize surface charge build

up, all spectra are referenced to C1s at 284.8 eV, and the background was subtracted by Shirley's method.

– Thermogravimetric Analysis (TGA): a TA Instruments Q500 thermogravimetric analyzer was employed using a quartz crucible for sample containment. The heating event consisted of a 10 °C per minute ramp to 1200 °C and a hold for 30 minutes at 1200 °C with weight measurements recorded every 0.5 s.

– Pressure Cell Combustion Investigations: product is tested in a closed system stainless steel combustion chamber. This technique, fully detailed by Sullivan *et al.* [42], employs ports connected to the chamber for live measurement of optical and pressure response during combustion. A thin nichrome wire heated by ramping a connected voltage source is used to ignite each shot. Pressure and optical data are recorded with an oscilloscope and managed with WaveStar software.

2.3 Results and Discussion

2.3.1 Product Inspection

Experiments with the reactor at 500 °C, an argon flowrate of 3000 sccm, and a bubbler temperature of 60 °C produced a light gray powder at the reactor outlet. Inspection of these particles via TEM showed a spherical particle product. Decreasing the furnace temperature to 350 °C yielded two particle morphologies: spherical and polyhedral. These systems, however, developed issues during product collection with clogging at the bubbler outlet due to condensation of precursor. To alleviate this issue, the stainless steel tubing at the outlet was sized up from 0.25 inch to 0.5 inch. The results showed a bulk product collection with more uniform morphologies; the system with a furnace temperature of 500

°C generated spherical particles whereas a temperature of 350 °C yielded primarily polyhedral particles, as shown in Figure 2.2.

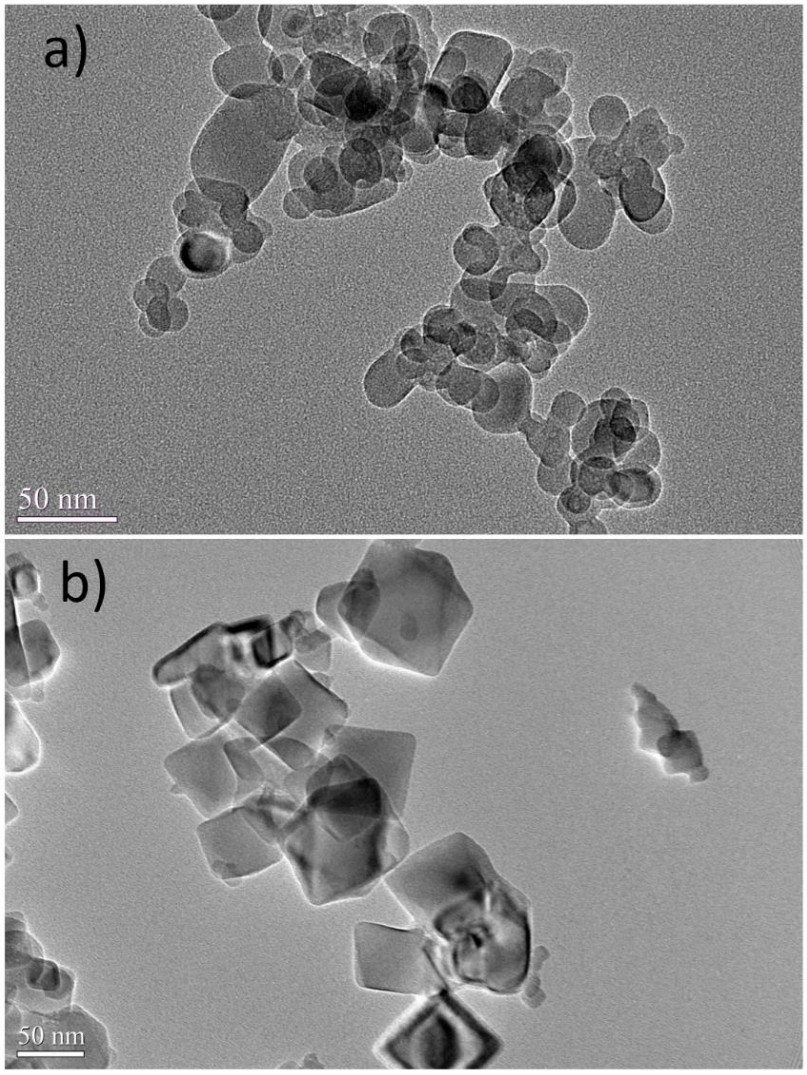

Figure 2.2: TEM image of Al particles produced at (a) 500 °C and (b) 350 °C.

TEM in Figure 2.2b displays particles of polyhedral structure with diagonal distances ranging from 50 to 150 nm for the furnace system at 350 °C and smaller spherical particles in Figure 2.2a with diameters ranging from 25 to 50 nm with the furnace at 500 °C. A small number of spherical particles are present in the polyhedral sample, and a count taken from lower magnification TEM sample images yields a particle count of 92.0 %

polyhedral. To investigate the composition of the polyhedral particles, high resolution TEM coupled with energy dispersive spectrometry (EDS) was employed, as shown in Figure 2.3.

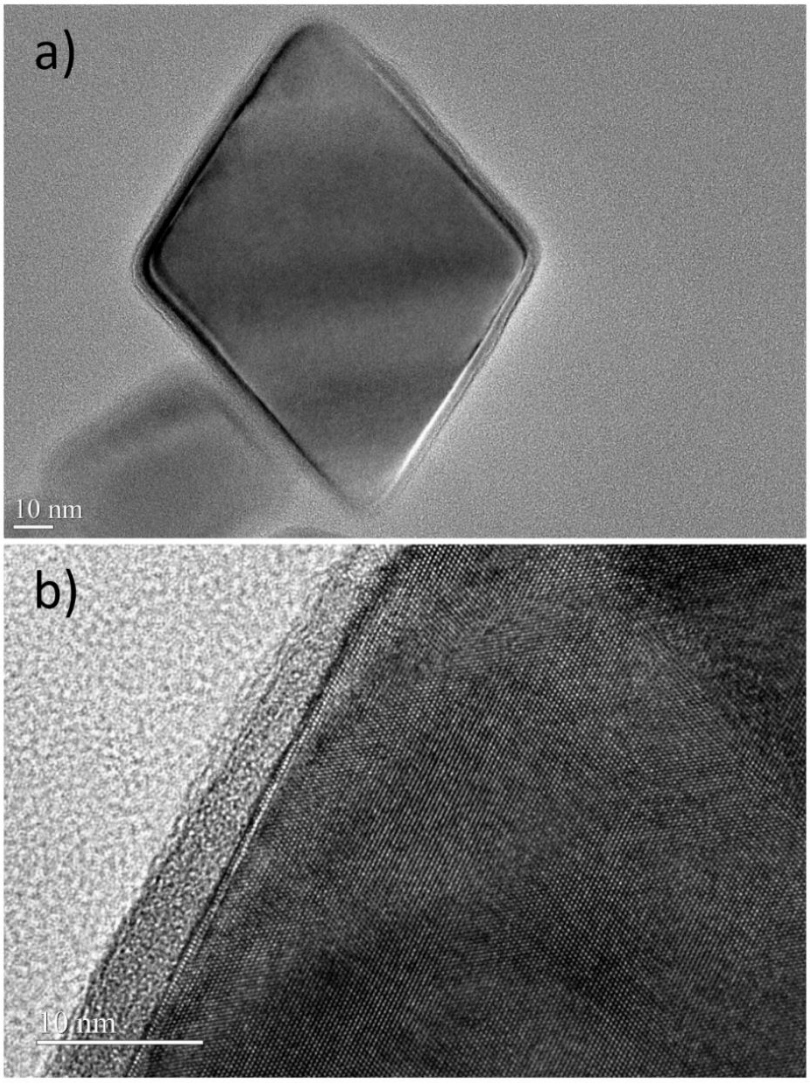

Figure 2.3: High resolution TEM images of (a) single polyhedral particle and (b) polyhedral particle edge showing a ~4 nm shell.

The high resolution images show the crystalline phase in the middle of the particle, as well as an amorphous coating of ~4 nm. Line spacing measurements of 0.228 nm in the crystalline phase are consistent with the literature value of 0.233 nm for <111> crystalline

aluminum. To confirm, EDS line scans and diffraction patterns were obtained for the product and are shown in Figures 2.4 and 2.5, respectively.

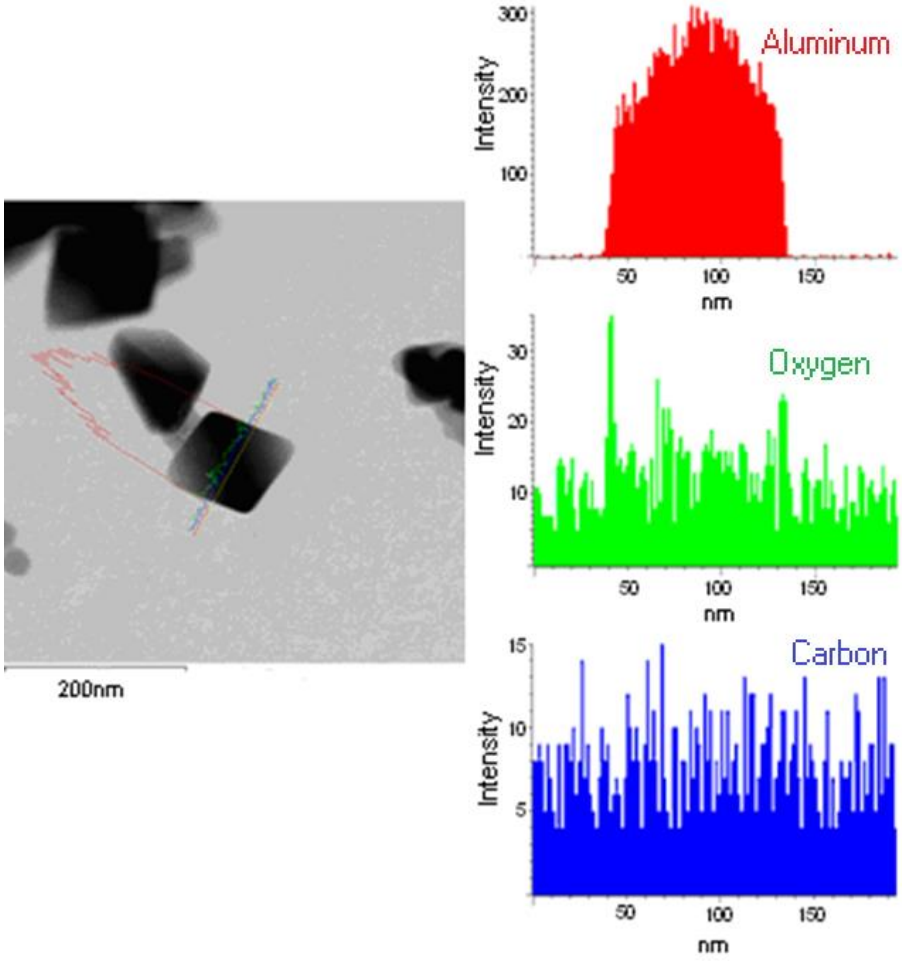

Figure 2.4: EDS linescan of polyhedral particle comparing aluminum, oxygen, and carbon intensities for particles deposited on Ni grid with SiO/SiO_2 film.

The line scan of a polyhedral particle in Figure 2.4 exhibits a clear peak of aluminum, no rise in carbon intensity, and a slight increase of oxygen intensity at the edges of the particle. The oxygen spectrum is likely indicative of an aluminum oxide shell, and the flat carbon scan suggests that the process has completely cracked the triisobutylaluminum precursor while keeping the resulting carbon containing compounds in the gas phase to pass through the collection filter.

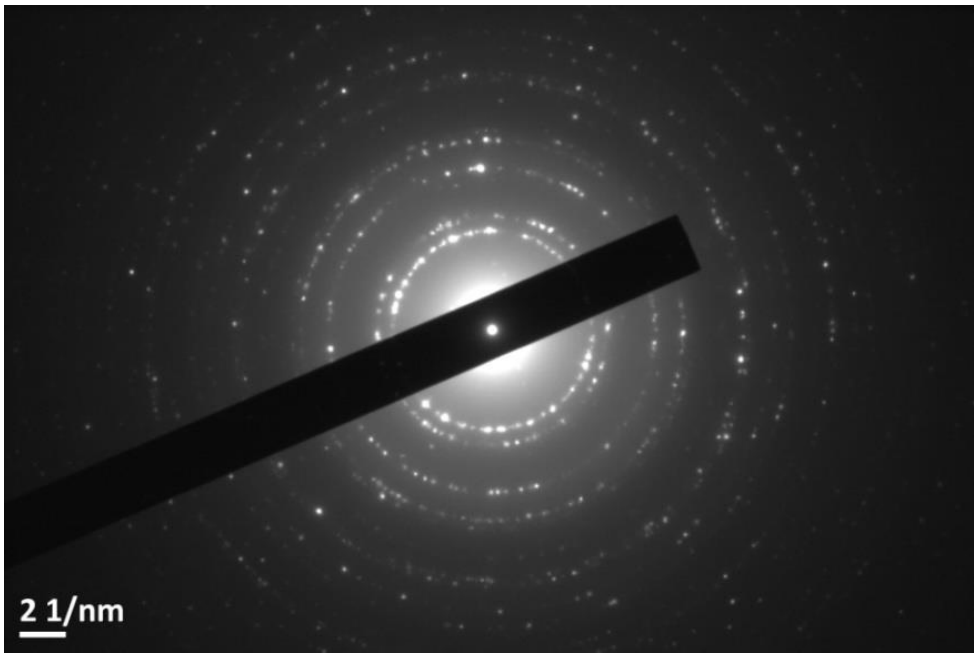

Figure 2.5: TEM X-ray diffraction image of polyhedral crystalline particle sample.

The experimental diffraction pattern shows clear diffraction rings, with the first three ring diameters from the center yielding lattice spacings of 0.239, 0.201, and 0.143 nm. These match with crystalline aluminum lattice distances of 0.233, 0.203, and 0.143 nm for the <111>, <200>, and <220> planes, respectively. This indicates clearly that this is primarily a crystalline aluminum product, but to characterize the amorphous shell shown in Figure 2.3 particle surface analysis is necessary.

With X-ray photoelectron spectroscopy, the top 1 to 10 nm of the particles is probed by irradiation and analysis of the electrons expelled. This penetration distance depends on the material density, but if the core crystalline aluminum is reached it can be ensured there has been a probe of the entire shell. The resulting Al2p spectrum is shown in Figure 2.6.

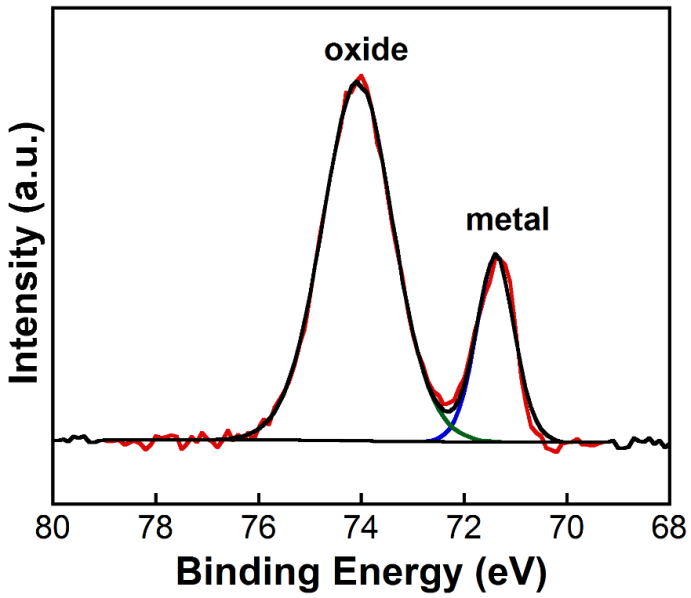

Figure 2.6: XPS aluminum spectra for synthesized product by thermal pyrolysis of triisbutylaluminum calibrated to Al2p at 71.4 eV.

This investigation clearly shows development of an aluminum oxide shell and this characterization has fully probed through the shell to reach the core metal. These observations combined with the measurements from the high resolution image lead to the conclusion that the polyhedral particles are crystalline aluminum with an amorphous aluminum oxide coating. This same particle morphology was previously shown by Haber *et al.* [35] during production of nanoAl by decomposition of aluminum containing compounds in solution. However, the previous work yielded polyhedral particles only as a small fraction of the product, whereas here they are the major component. The key to production of mainly polyhedral crystalline particles is the low temperature synthesis allowing the particles to grow into the single crystalline form.

In-line size distributions of the aerosol polyhedral aluminum product were measured using the scanning mobility particle sizer apparatus, detailed previously. Sizing

data are fit to a lognormal distribution based on the measured total particle concentration, geometric mean diameter, and standard deviation as shown in Figure 2.7.

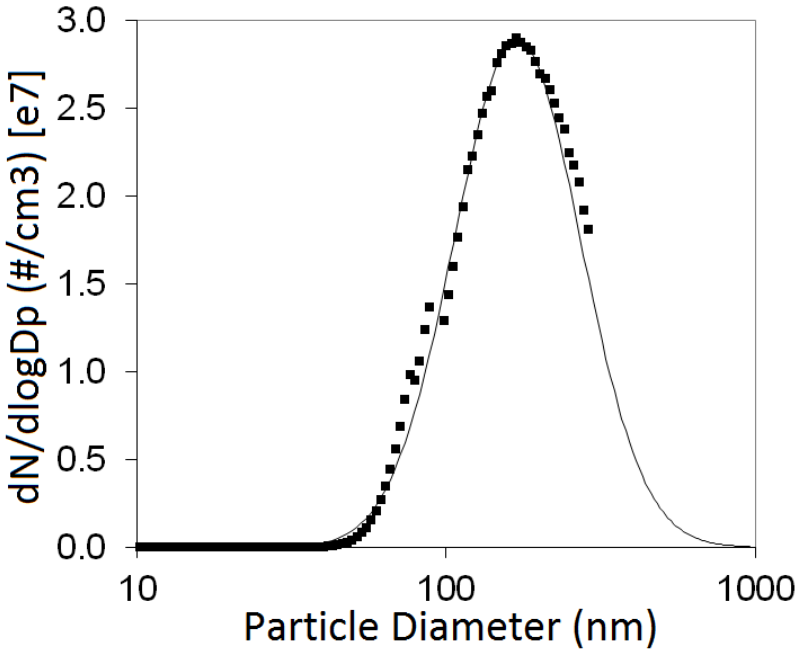

Figure 2.7: SMPS experimental distribution and lognormal fit of polyhedral aluminum product from TibAl thermal pyrolysis.

During testing with the differential mobility analyzer as part of the SMPS system, high voltages required to separate large particle sizes can result in electric arcing for large particle concentrations. An arc shuts down the SMPS system, as seen for particle sizes above 300 nm in Figure 2.7, but enough of the distribution is probed for this case to properly fit the lognormal distribution for full analysis. This lognormal particle size distribution is based on measured parameters for total particle concentration, N, standard deviation, σ_g, measured particle size, D_p, and mean particle diameter, $D_{p\text{-mean}}$, as shown in Equation 4.

$$\frac{dN}{d\ln D_p} = \frac{N}{(2\pi)^{1/2}\ln\sigma_g}\exp\left(-\frac{(\ln D_p - \ln D_{p-mean})^2}{2\ln^2\sigma_g}\right) \quad (4)$$

Results show a mean diameter of 162 nm with a total mass flow of $1.3 \cdot 10^{-2}$ g/min, indicating a high experimental production rate of aluminum. Comparing to predicted theoretical production rates in Table I of $1.2 \cdot 10^{-2}$ g/min I actually have a slightly higher experimental aluminum yield, but this can be attributed to potential inaccuracy from limited vapor pressure data for this triisobutylaluminum precursor. The SMPS characterization, however, does not give a clear description of the product primary particle size due to aggregation in the aerosol phase. In order to create a proper description of the primary particle size distribution, sizes were measured from TEM results to create a histogram. This approach yielded a distribution with average primary particle size of 87.5 nm and a standard deviation of 32.9 nm. Due to the polyhedral shape of the particles, the long diagonal distances from these bipyramidal particles were used as the descriptive size measurement for each particle. Since the TEM grids are open to air after collection, this distribution is for aluminum particles that have formed a thin aluminum oxide coating.

The spherical particles seen in Figure 2.2a were originally hypothesized to be amorphous carbon contamination particles that had formed during the cracking of TiBAl. However, attempts at carbon reduction by hydrogen addition at concentrations of up to 10 mass percent showed no discernable effect. To evaluate the phase and structure of these particles, high resolution images of the spherical particles were acquired, as shown in Figure 2.8.

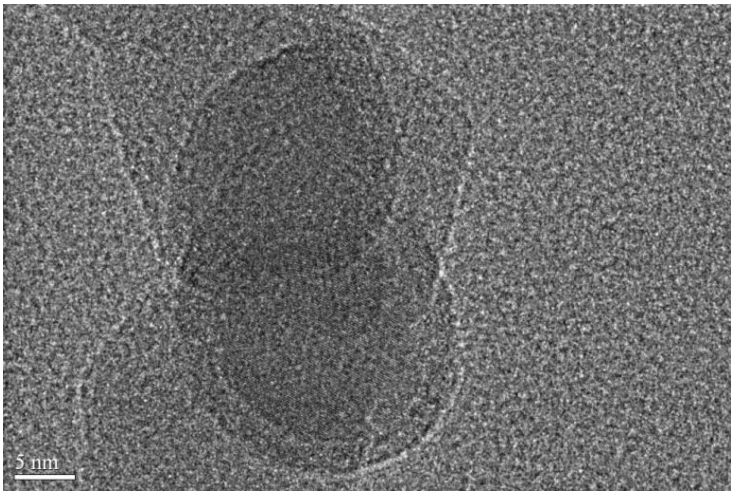

Figure 2.8: High resolution TEM image of spherical particle product.

The high resolution image shows a mostly amorphous character, with small scattered sections displaying crystalline lattice fringes. This information suggests either an amorphous aluminum or formation of aluminum oxide upon exposure. For supplemental characterization to determine this difference, EDS is assessed in Figure 2.9.

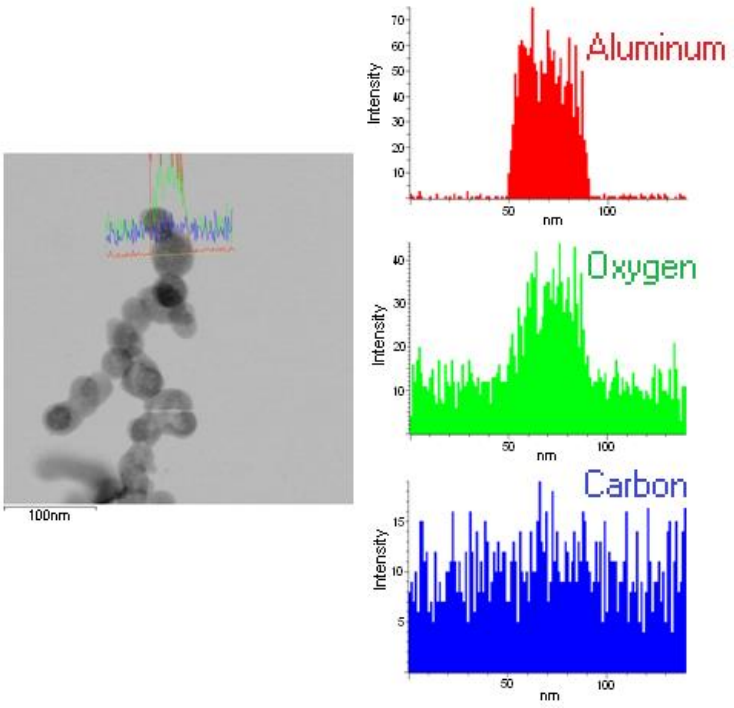

Figure 2.9: EDS linescan of spherical particle comparing aluminum, oxygen, and carbon intensities for particles deposited on Ni grid with SiO/SiO_2 film.

The EDS elemental line scan in Figure 2.9 supports evidence that these are aluminum oxide with relatively no carbon contamination. Since oxygen is not available to the particles until the outlet of the production system, it can be concluded that these small spherical aluminum particles are extremely reactive and that even with a slow oxygen bleed after product collection they have in most cases fully reacted with oxygen upon exposure. There are still parts in the core of some of these particles that remain unreacted aluminum, as evidenced by some crystal lattice lines in the high resolution images. This is further indication that these spherical particles were pure aluminum before exposure and reaction with oxygen. When process conditions yield mostly these spherical particles, the resulting samples react completely with oxygen upon exposure, even after the slow air bleed. Samples produced with mostly polyhedral crystalline particles, however, remain stable upon exposure after the bleed, suggesting that these crystals have higher stability than the spherical particles. The stable nature can be attributed to the higher surface binding energy for molecules on a flat surface compared to that of a curved surface due to the Kelvin effect [26].

2.3.2 Reactivity Investigation

As a majority of the active fuel content in the small spherical particles is lost to oxidation immediately upon exposure, additional analysis of these samples was not necessary for particle sizing and reactivity. The highly faceted crystals remain stable and are thus more likely to be a useful product. The polyhedral morphology could potentially lead to novel reactivity results compared to a traditional spherical aluminum.

In order to further investigate the reactivity of the polyhedral crystalline particles, thermal gravimetric analysis under air was employed to further scrutinize polyhedral

particle samples, specifically to determine the remaining active aluminum content after particles had formed an oxide shell. Resulting mass measurement is shown in Figure 2.10 as temperature is raised to 1200 °C at 10 °C/min then held for 30 minutes.

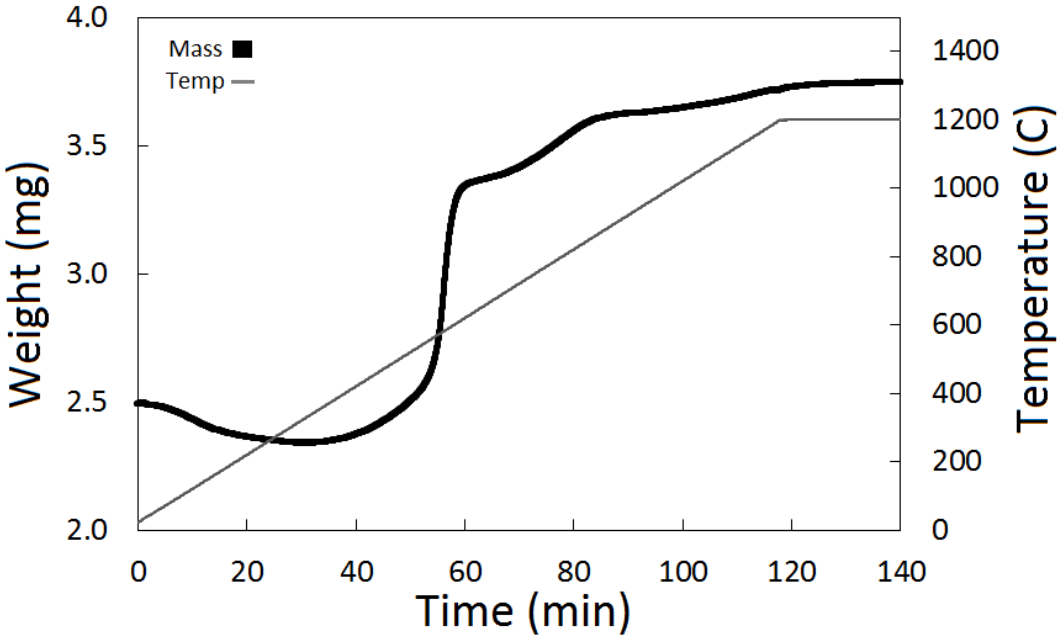

Figure 2.10: TGA heating results for synthesized Al sample.

Calculation based on mass change shows an active aluminum content of 63.9%. This result is consistent with theoretical calculations for active content of an 87 nm particle of bipyramidal shape with a 4 nm aluminum oxide layer showing a percentage of 65%. The content is slightly lower but comparable to a 70% content measured for commercial nanoAl of average diameter 50 nm in TGA. These tests give sample information for a slow heating event, but further investigation is necessary to evaluate the performance of this material in a fast combustion process.

Samples were combined in thermite mixtures with a stoichiometric amount of CuO nanoparticles and burned in 25 mg shot samples in the pressure cell, described previously. Three relevant pieces of information are obtained from these measurements including the

peak pressure, the pressurization rate, and the optical response. The latter two provide a qualitative measure of burn time, while the former is a measure of the gas generation presumably from the oxygen release from oxide, a theory described by Zhou *et al.* for metastable intermolecular composites [43]. The burn time is evaluated as the FWHM of the optical response. Combustion tests were performed in the cell for stoichiometric thermite mixtures of synthesized Al/CuO and commercial Al/CuO. The commercial nanoaluminum consists of average sized 50 nm spherical particles as reported by the Argonide Corporation supplier and confirmed by TEM inspection.

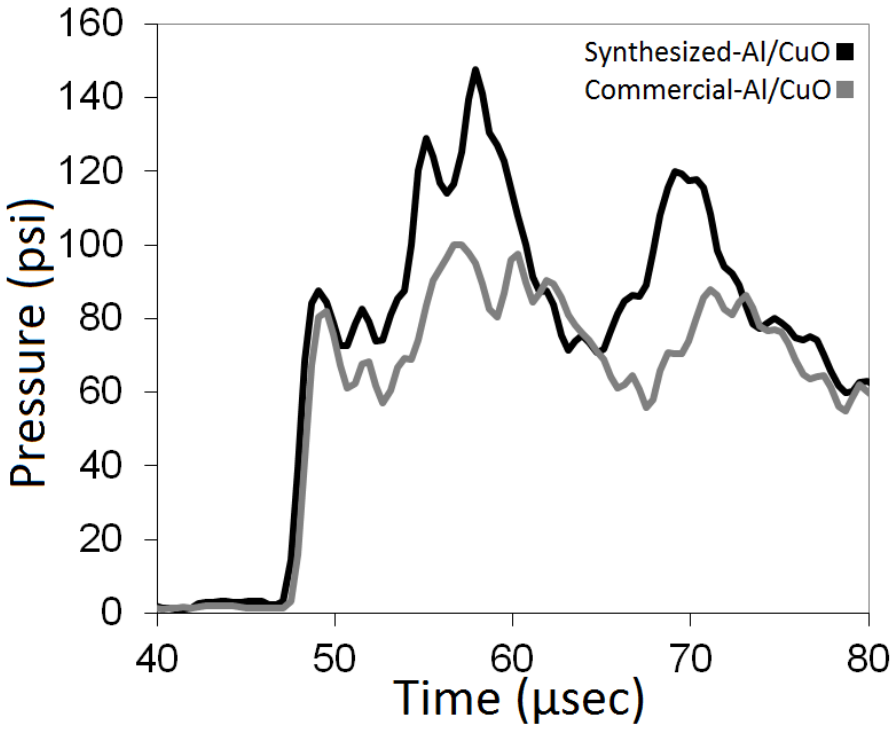

Figure 2.11: Combustion cell pressure response comparing synthesized Al to commercial Al; both combined in stoichiometric thermite mixture with CuO.

Pressure response from these experiments showed a maximum pressure rise of 148 psi for the synthesized Al compared to a value of 100 psi for commercial product, both

with similar rise times. The polyhedral particles thus yield a significant enhancement in reactivity.

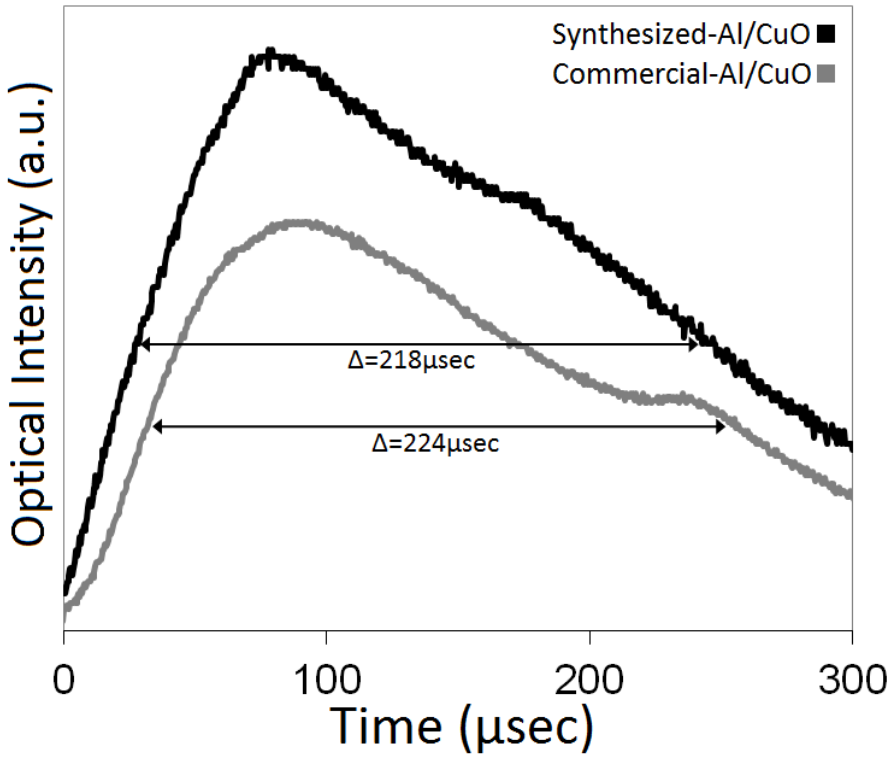

Figure 2.12: Combustion cell optical response comparing synthesized Al to commercial Al; both combined in stoichiometric thermite mixture with CuO.

Though a broader peak seems apparent for the synthesized aluminum, FWHM calculations reveal similar characteristics for burn time. The higher intensity peak for the synthesized sample can be attributed to a brighter combustion event as a result of the increased energy release displayed in pressure response. This information combined with experimental observations leads to the conclusion that this process has produced air stable polyhedral nanoaluminum particles that can release a higher amount of energy in the same time frame. This enhancement is displayed by this polyhedral nanoaluminum sample despite TGA evidence of a lower active aluminum content.

2.4 Conclusions

A low temperature gas-phase pyrolysis of TiBAl was used to produce phase pure bare aluminum aerosol nanocrystals. TEM shows spherical particle morphologies for synthesis at 500 °C and polyhedral crystalline morphologies for production at 350 °C. The crystalline particles form a ~4 nm oxide shell after exposure to air, and combustion studies lead to the conclusions that these polyhedral nanoaluminum particles have stability and an increased energy release. Though the bare nanoaluminum in these experiments was passivated with oxygen, this system could easily be coupled with other systems to coat the bare aluminum with other materials for specific energetic applications.

Chapter 3: Ni/Ni_2O_3 Coating of Aluminum

3.1 Literature Review

As previously detailed, coating aluminum with thin layers of metals and metal oxides has garnered significant interest showing potential to alter reaction mechanisms during combustion. Developing a coating of nickel or nickel oxide could potentially protect the core aluminum from oxidizing, alleviating concerns with the alumina shell's impediment to reaction. If the metallic nickel layer is kept from oxidizing completely upon exposure, an exothermic alloying process between aluminum and nickel during combustion could decrease ignition temperature [17,19]. If the thin coating layer oxidizes completely upon exposure, it could still prove useful by acting as a local oxygen lender to aluminum during combustion.

Common approaches for nickel nanoparticle fabrication include the gas evaporation method (GEM) [44,45], sputtering [46], various chemical methods in solution [47-49], sol-gel [50], and laser decomposition of gaseous $Ni(CO)_4$ [51]. Chemical and sol-gel techniques, though reliable sources of nanoNi, were not easily tunable to create an experiment for Ni coating aerosolized Al. Previous work by Zhou *et al.* produced Ni nanocrystals from $Ni(CO)_4$ via gas phase thermal pyrolysis [52]. Familiarity with the gas phase thermal pyrolysis method and ease of incorporation into an aerosol based coating scheme led to its selection. The $Ni(CO)_4$ gas can be combined with the Al aerosol product and subsequent decomposition in a furnace could potentially yield a homogeneous coating of Ni on the Al crystal surface. This in-situ coating technique allows the whole system to remain a continuous aerosol flow so it can be easily scaled up to low cost large-scale manufacture if the coated product is proven valuable.

3.2 Experimental Setup

3.2.1 Ni/Ni_2O_3 Coated Aluminum Synthesis

The nickel production system adopted from the work of Zhou *et al.* [52] in my research group involves the formation of $Ni(CO)_4$ gas and subsequent decomposition in a furnace at 420 °C. To produce nickel tetracarbonyl, a flow of 50 sccm carbon monoxide is sent through a 25 inch bed packed with micron sized nickel powder (Sigma-Aldrich) brought to 50 °C by heating tapes. The outlet is combined with the aluminum aerosol mass flow of $1.3 \cdot 10^{-2}$ g/min and sent to the second furnace reactor for decomposition of $Ni(CO)_4$. Process tubing is connected to two 0.5 inch diameter quartz tubes, heated within a 15.5 inch tube furnace. Flow rates of 1500 sccm through the coating furnace yields residence times of 2.0 s as shown in the experimental setup in Figure 3.1.

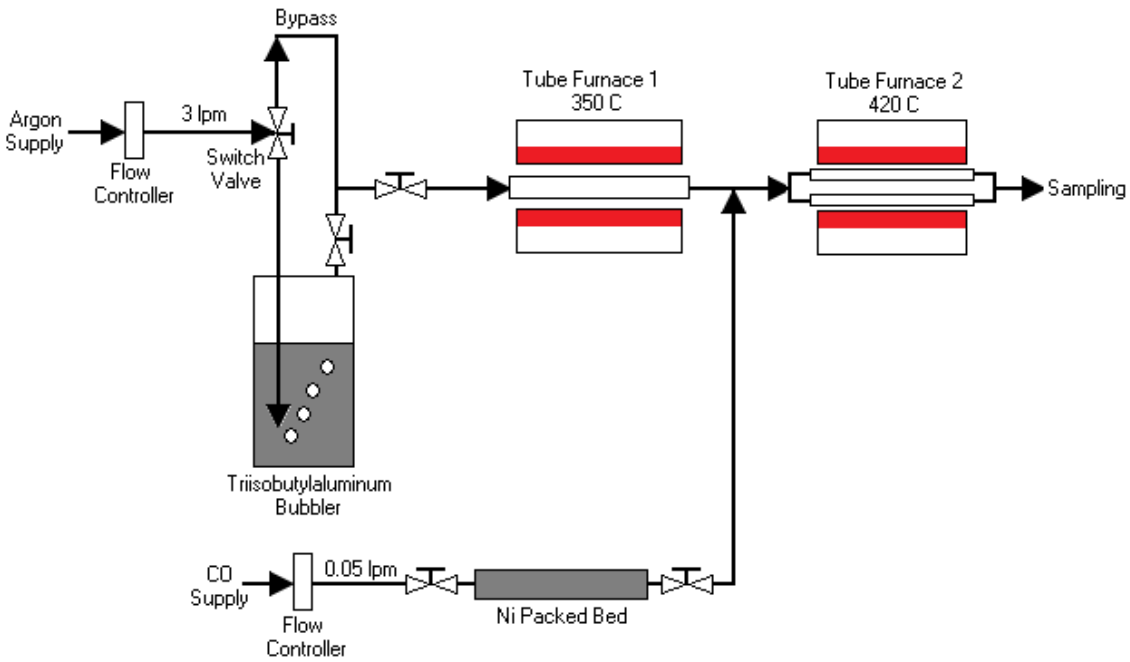

Figure 3.1: Experimental setup for coating of Al by decomposition of nickel tetracarbonyl.

Prior to running the system as shown, hydrogen is used to clean the surface of the nickel powder in the packed bed. A hydrogen cylinder is connected in place of the carbon monoxide source, and H_2 gas is sent through the bed while heating to 350 °C for a duration of four hours. This task must be accomplished prior to each run of the nickel tetracarbonyl system. As nickel tetracarbonyl is highly toxic, all lines must be cleared with argon after production and sent through a furnace for complete decomposition. The formation and decomposition of nickel tetracarbonyl ensures complete safety in this process. After collection of sample, a slow bleed of air ensures proper stability before opening the filters to harvest product.

3.2.2 Product Evaluation Apparatus

– SMPS, HRTEM/EDS, XPS, and Pressure Cell Combustion: these systems are detailed previously in Section 2.2.2

– Wire Temperature-Jump Ignition and High Speed Video: these apparati are employed in cooperation to determine ignition temperatures of fuel product samples in stoichiometric thermite combination with CuO nanoparticles (<50 nm, Sigma-Aldrich). Samples are sonicated in hexane for 30 minutes and deposited on a 76 μm diameter platinum wire with a total heated length of ~12 mm, as detailed by Zhou *et al.* [53]. Combustion is initiated by connecting the wire to a high voltage power source varied by changing the pulse voltage, resulting in heating rates of ~$4 \cdot 10^5$ K/s, with the wire replaced after each heating test. A Phantom V12 high speed digital camera monitors the combustion behavior of the nanothermite on the wire. Measurements are recorded for voltage and transient current through the circuit, and wire resistance measurements allow for real time temperature information throughout the event.

3.3 Results and Discussion

3.3.1 Product Inspection

To obtain a theoretical coating thickness based on production of nickel, particle size distributions were measured using the SMPS system detailed previously. Conditions with a $Ni(CO)_4$ decomposition furnace temperature of 420 °C for production of nickel without aluminum yielded the distribution shown in Figure 3.2, along with the original uncoated aluminum distribution.

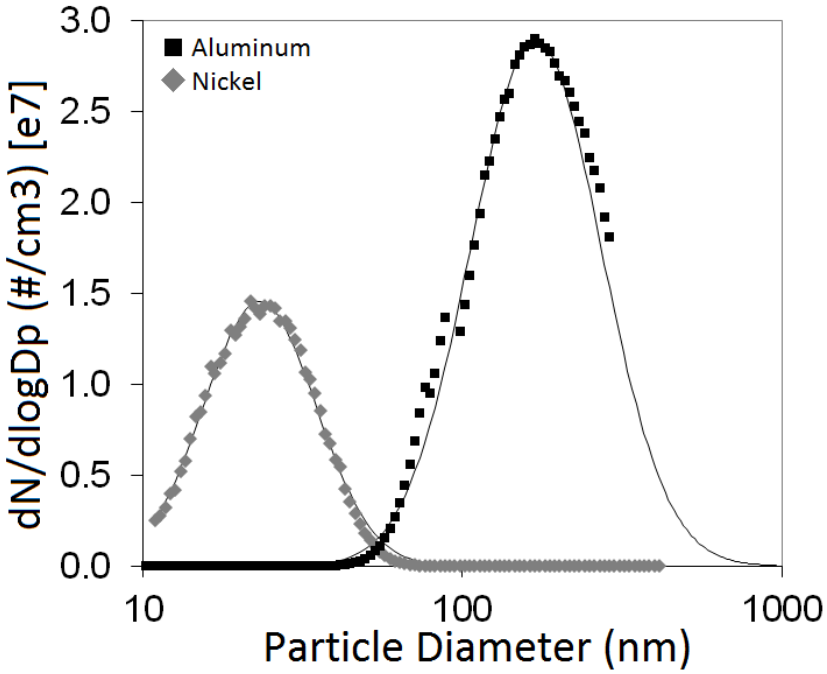

Figure 3.2: Experimental and lognormal fit product aerosol size distributions for Ni and Al, measured separately.

SMPS measurements are fit to lognormal distributions to give the results shown. Assuming 100% condensation of nickel onto the aluminum nanoparticle surface, the coating thickness on the aluminum core can be estimated. The mass ratio of Al to Ni based on these experimental results gives a value of 0.38, resulting in a coating thickness of 3.2

nm Ni. Though some nickel will oxidize upon exposure, the goal is to maintain some metallic nickel in the core to perform the alloying reaction with aluminum during combustion. Product from the nickel coating setup was collected on TEM grids with the aerosol sampler and analyzed with high resolution TEM, as shown in Figure 3.3.

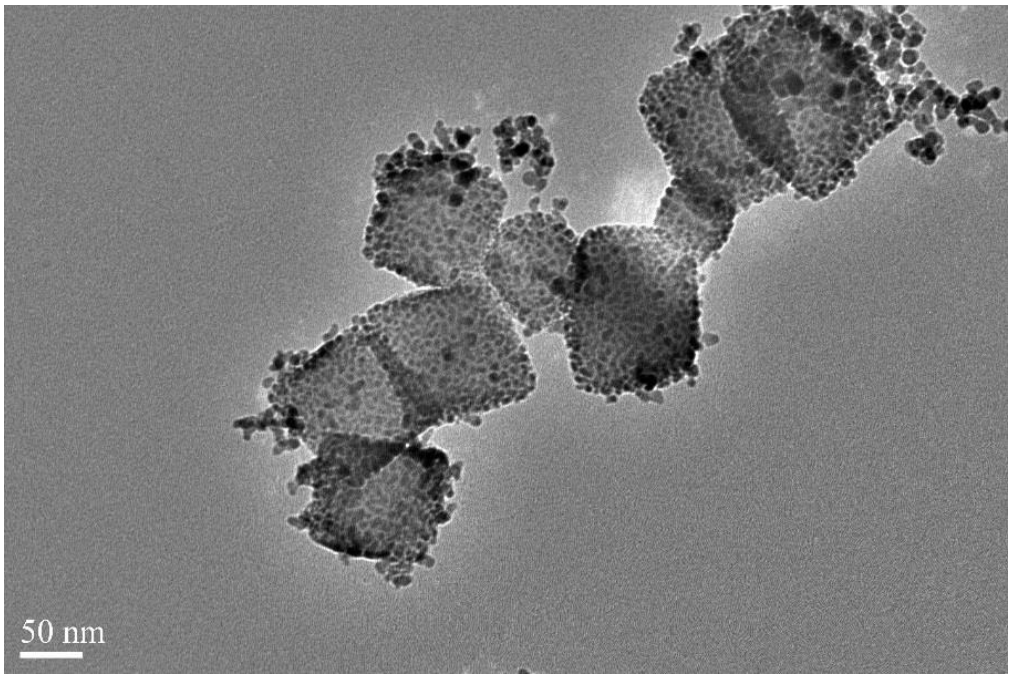

Figure 3.3: TEM image of particles produced from nickel tetracarbonyl decomposition and deposition on Al.

Inspection shows the polyhedral nanoaluminum particles decorated with small 5-10 nm particles, suspected to be nickel. It is clear that a homogeneous coating of nickel has not been accomplished, rather a heterogeneous coating of particles on the surface. Though the goal was to obtain a thin layer coating of nickel as opposed to this small particle decoration, it is worth investigating if this material could still prove useful. Energetic enhancement could be shown by protection from oxygen penetration or a potential exothermic alloy reaction between aluminum and nickel. In order to evaluate the

composition of this material, EDS line scans were employed to obtain spectra across a whole aluminum particle, as shown in Figure 3.4.

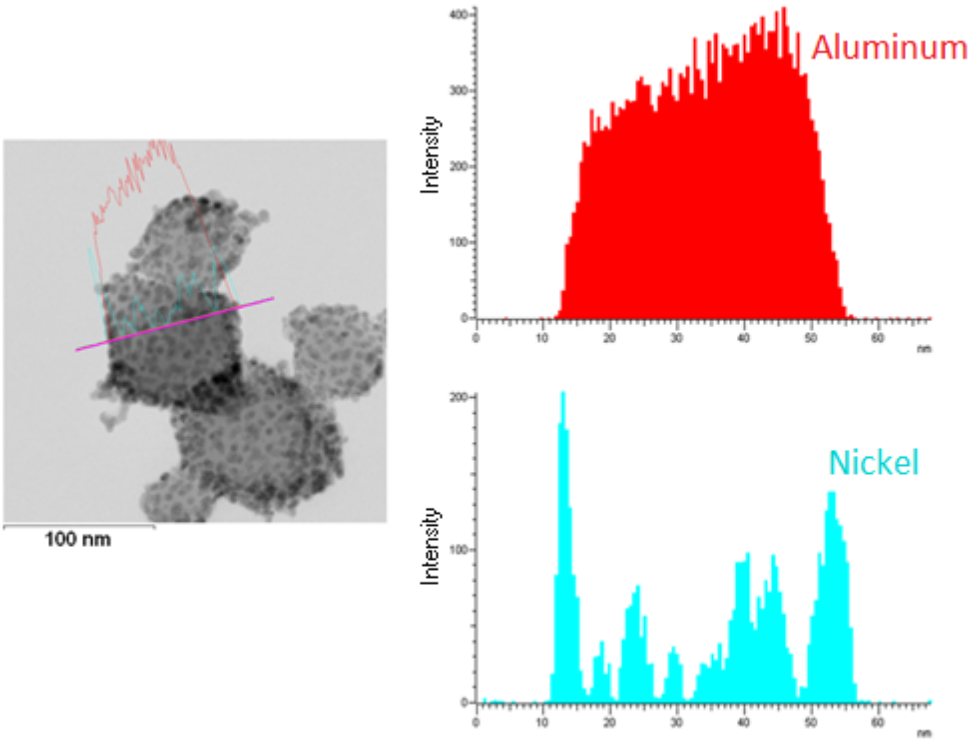

Figure 3.4: EDS linescan of a coated aluminum particle.

As expected, the small particles on the surface of the aluminum are confirmed to contain nickel. The nickel tetracarbonyl decomposition has been completed in the reaction furnace, and the gaseous nickel has a high enough concentration to condense and nucleate into individual particles that subsequently attach to the aluminum surface. Electron dispersive spectroscopy has confirmed the presence of nickel in these particles, but this technique cannot determine if they contain metallic nickel or if all of it has been oxidized upon exposure. To further investigate the structure of the decorated particles, ultra high resolution images were acquired with a focus on the particle edge. If metallic nickel is present, it can be confirmed with lattice spacing measurements

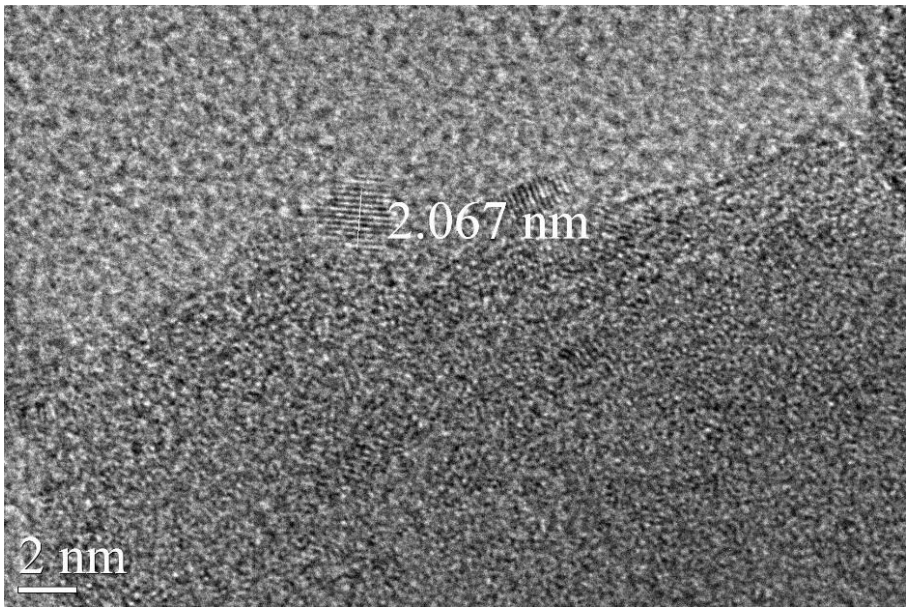

Figure 3.5: High resolution TEM image of a coated aluminum particle with lattice spacing measurement.

TEM images do reveal some lattice fringes present in the small particles covering the aluminum. A measurement of 0.2067 nm for the lattice spacing is consistent with an interplanar spacing of 0.2035 nm for pure Ni(111) [54]. The other amorphous material present in the dotted coating can be attributed to nickel that has oxidized upon exposure to air, but its amorphous nature means it cannot be identified via lattice spacing measurements. Since some metal remains on the interior, there is potential to alloy with aluminum during combustion, but the scarcity of these crystalline sections would make it unlikely to be a large contributor energetically. The nickel oxide could also act as an oxidizer during a combustion reaction. Attaching it on the aluminum surface could enhance reactivity by direct delivery of this oxidizer.

The particle coating is accomplished in an oxygen free environment via the argon based aerosol process, but further analysis is required to determine if the coating has protected the aluminum core from oxidizing after exposure. XPS was employed to locally

characterize the edge of the particle by analysis of electrons expelled from the top 1 to 10 nm of the particle during irradiation, with this penetration distance largely depending on the density of the material. Resulting plots for the Al2p spectra are shown in Figure 3.6 compared to uncoated synthesized aluminum crystals.

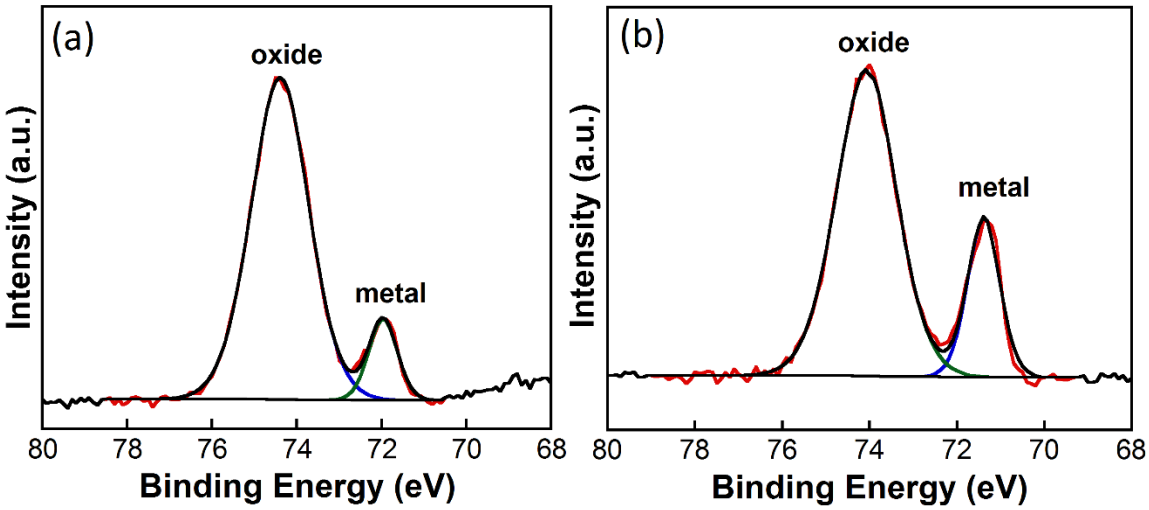

Figure 3.6: XPS aluminum phase results for (a) Al coated via nickel tetracarbonyl decomposition and (b) uncoated synthesized Al.

As expected due to the heterogeneous coating of nickel particles on the surface, oxygen has reached the aluminum core, as made evident by the appearance of a significant aluminum oxide peak in Figure 3.6a. Though nickel particles seem to be covering the entire surface, there are bound to be pathways for oxygen to penetrate in such an arrangement. In addition, the relative peak heights for aluminum metal to aluminum oxide for the coated case compared to uncoated aluminum shown in Figure 3.6b indicate a thicker aluminum oxide layer for the nickel coated material. Thus heterogeneous coating has not passivated the core aluminum particles, it has facilitated formation of a slightly thicker oxide layer.

An understanding of the metal oxidation processes involved can explain the formation of this increased oxidation of aluminum. During the slow bleed of air/argon into

the filter collected product, oxygen is able to pass between the nickel particles to access the interior bare aluminum. At the same time, oxygen is also reacting with nickel to form nickel oxide. Since this nickel oxidation process produces a significant amount of heat, it subsequently increases the temperature of the whole particle surface. A higher temperature of the aluminum surface will increase the diffusivity of the constantly forming alumina shell, and thus oxygen can penetrate further before the barrier to diffusion is too high. To investigate the exact phase of the nickel material on the surface, the Ni2p spectrum from XPS can be analyzed, shown in Figure 3.7.

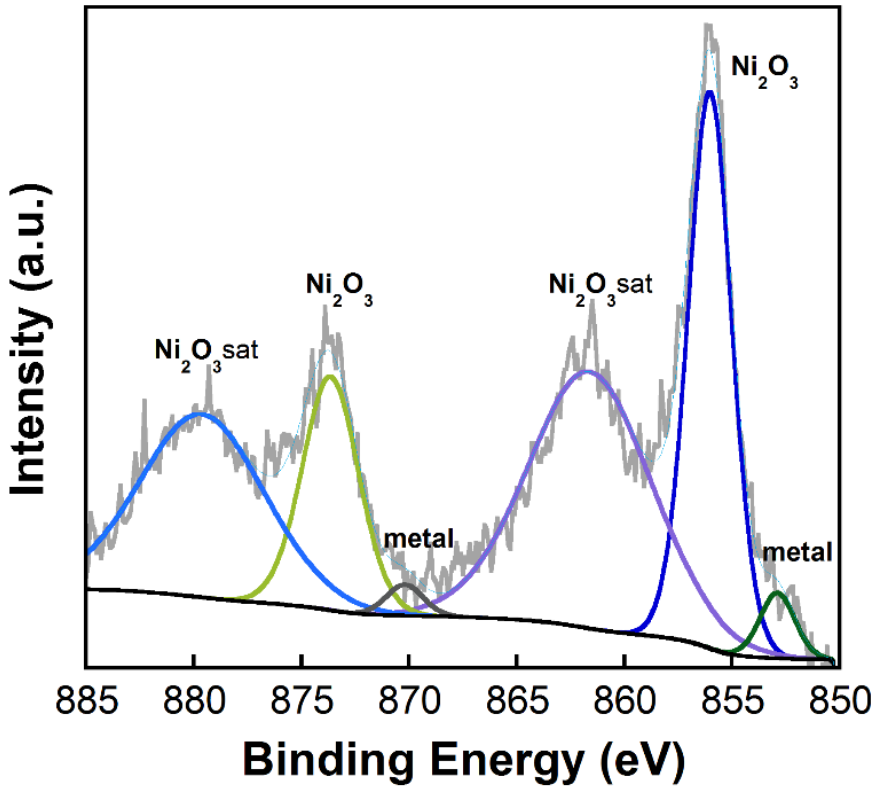

Figure 3.7: XPS results for Al coated via nickel tetracarbonyl decomposition showing the phases of nickel.

The XPS spectrum shows multiple phases of nickel. Peaks match with metallic nickel as well as the Ni_2O_3 phase, as matched to literature values [55]. The high intensities

for the Ni_2O_3 phases indicate a much larger percentage of the oxide compared to the metal, and since aluminum is present in the previous Al2p spectra it can be ensured that the experiment has probed the entire coating layer. Calculations for the percentage of nickel metal to nickel oxide based on these data reveal that the oxide is by far the majority of the material, with the metallic nickel only composing 3% of the coating layer. This matches with high resolution TEM imaging observations shown in Figure 3.5 indicating a large amount of amorphous material with scattered sections of crystalline nickel. This small percentage of metallic nickel would make any alloying between the two metals a negligible contributor to a combustion event.

Thus is has been found that the product from the nickel tetracarbonyl decomposition scheme has a yielded a heterogeneous decorated coating of small particles, a majority of which have oxidized to form Ni_2O_3, and this coating has not protected the aluminum core from oxygen penetration. Despite these factors, it is still worth exploring if the addition of an oxidizer at such close proximity to aluminum will yield an increased reactivity during full combustion of product.

3.3.2 Reactivity Investigation

To examine the reactive properties of the coated aluminum, bulk product was collected from the nickel tetracarbonyl coating experiment using polypropylene filters. This material was combined with a stoichiometric amount of nanosized CuO (Sigma-Aldrich) based on calculations for active aluminum percentage considering a 5 nm nickel oxide layer and a slightly thicker alumina layer as was indicated by the aluminum XPS spectra in Figure 3.6. This results in a much lower theoretical active aluminum content of 33.2% compared to the uncoated aluminum experimental result of 64%. The high density

of nickel and nickel oxide in such a thick layer is the main contributor to this factor. If the nickel oxide acts as an oxidizer during combustion, however, this coating layer can take the place of some of the CuO in the thermite combination. As it is not known how much oxygen will be provided by nickel oxide during combustion, a range of percentages of CuO are added to evaluate the ideal ratio for maximum energetic response.

These mixtures were then ignited in the combustion cell experiment, detailed previously, to evaluate optical and pressure response during the reaction. Acquired data for the highest reactive mixtures are compared to uncoated synthesized aluminum thermite in Figures 3.8 and 3.9 for pressure and optical response, respectively.

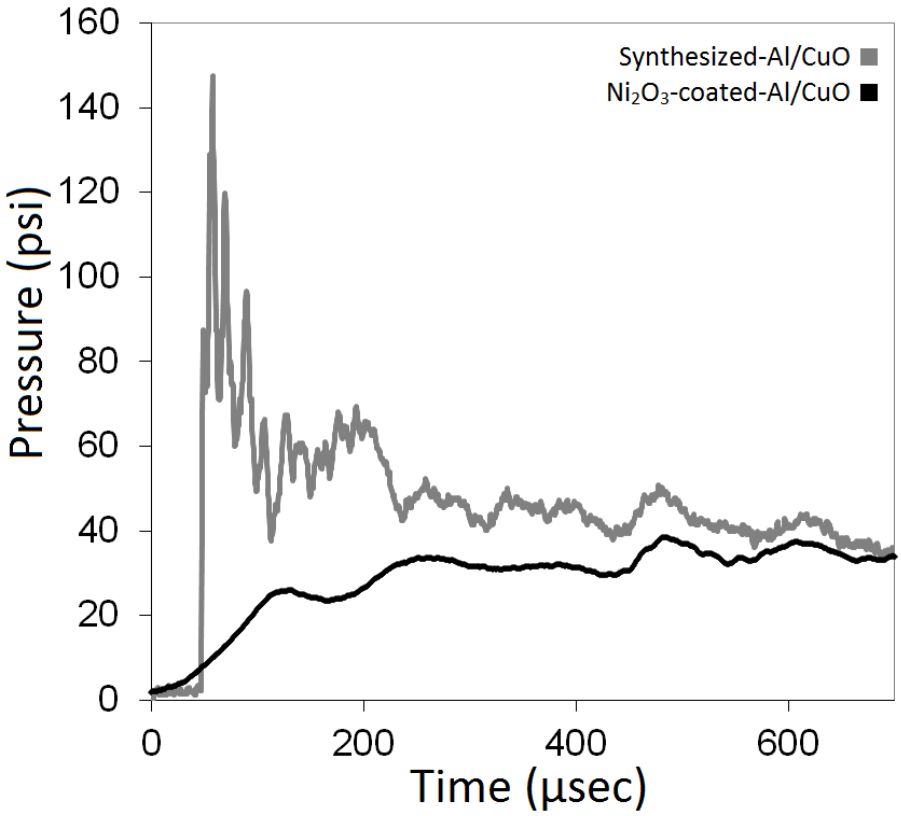

Figure 3.8: Combustion cell pressure response comparing Ni_2O_3 coated Al and uncoated Al in thermite combinations with CuO.

These plots indicate a drastic decrease in reactivity for the coated case, and calculations based on the pressure response acquired data exhibit a pressure rise of 39 psi, a radical reduction from the 148 psi for uncoated aluminum. Burn times based on the FWHM of the optical response also indicate poor reactivity with a value of 420 µsec compared to the uncoated Al case exhibiting a 218 µsec burn time. This result is for the coated sample mixture containing a near proportionate amount CuO considering all oxygen from Ni_2O_3 is delivered to aluminum during combustion, with all other percentage combinations yielding lower reactivity responses. The oxide coating layer is likely to be performing as an oxidizer, but this direct delivery has not resulted in an enhanced pressure response or burn time; it has hindered the combustion event.

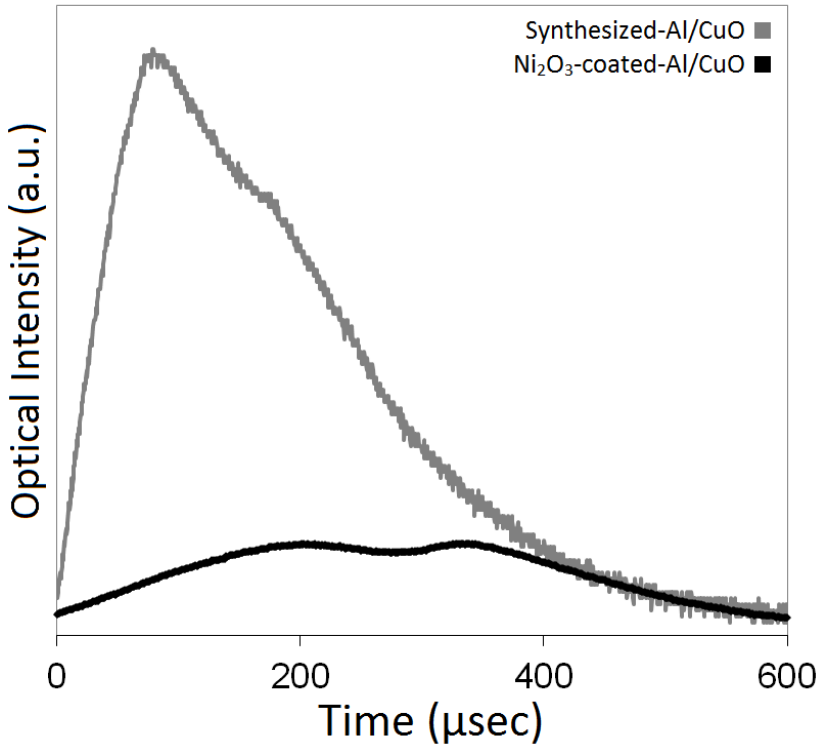

Figure 3.9: Combustion cell optical response comparing Ni_2O_3 coated Al and uncoated Al in thermite combinations with CuO.

Though energy release does not show improvement for the coated material, wire heating investigations were undertaken to explore if any information could be extracted about the viability of a reduced ignition temperature, as has been predicted for nickel-aluminum systems in literature [17,19]. Calculations based on the time of ignition matched to wire resistance measurements averaging three runs with a heating pulse of ~3 ms yield an ignition temperature of ~923 K for the nickel oxide coated aluminum, a significant reduction compared to the uncoated aluminum result of ~1057 K. These results, both with standard deviations under 20 K, represent a considerable improvement, and suggests that a thinner coating layer that doesn't significantly hinder energy release could yield a useful fuel product. The reduced ignition temperature witnessed here could be attributed to a possible alloying process involving nickel oxide and aluminum, a process that could differ significantly from Ni-Al alloying.

Thus, the product from the nickel tetracarbonyl decomposition coating scheme has yielded a decoration of particles on the aluminum surface, shown by XPS to be primarily composed of Ni_2O_3. This coating has facilitated increased formation of aluminum oxide and demonstrated poor energetic response during combustion. This product has a low fuel content and the coating does not perform well as an oxidizer, but decreased ignition temperature measurements indicate a potential enhancement. If a homogeneous layer coating of nickel oxide is produced, these experiments could prove successful.

3.3.3 Further Coating Attempts

Additional experimentation was necessary to attempt a homogeneous coating on the surface of the bare aluminum particles. Though observations from the previous testing show it is unlikely to keep a significant amount of metallic nickel from oxidizing, a

homogeneous coating could protect the aluminum core from oxidizing upon exposure. Process issues limit the ability to decrease the nickel concentration as there is already an extremely low flow through the nickel packed bed, and lowering the bed temperature yields similar results in nickel particle decoration on the aluminum surface. Therefore, further effort to attempt a homogeneous coating involves the decreasing of the nickel tetracarbonyl decomposition furnace temperature.

To find the appropriate coating furnace temperature, the furnace setpoint is decreased stepwise from 420 to 180 °C, measuring total particle concentrations at each step with the condensation particle counter. This experiment consists of a closed aerosol system, but due to safety concerns with the toxicity of nickel tetracarbonyl, lower temperature tests are completed in the fume hood to avoid any accidental exposure. Measurements at a temperature of 200 °C show a steep drop in total concentration, indicating the ideal setting for homogeneous nucleation of nickel on the aluminum surface. Samples are collected and inspected in the TEM microscope, as shown in Figure 3.10.

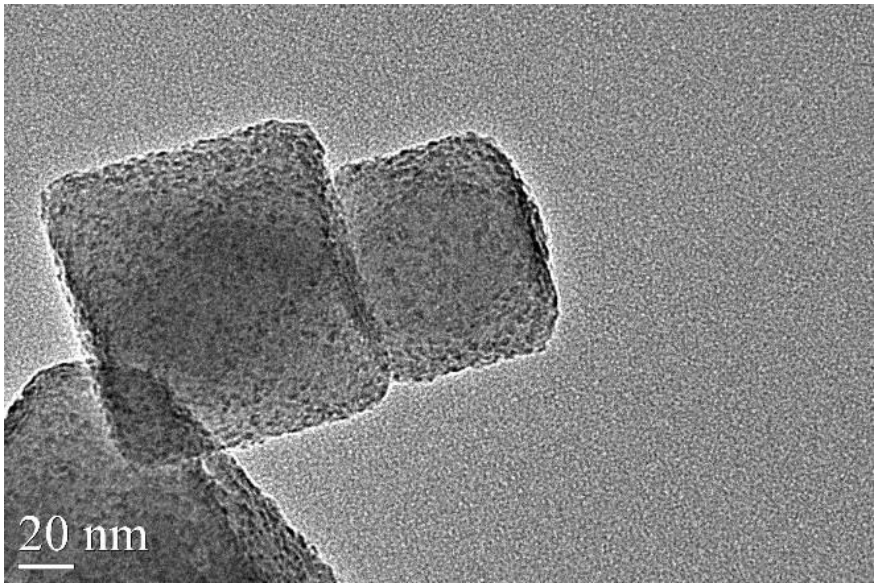

Figure 3.10: TEM image of product from aluminum coating experiment with nickel tetracarbonyl decomposition at 200 °C.

Close inspection shows that at 200 ℃ there are still individual particles on the aluminum surface; the system still yields heterogeneous nucleation. At temperatures below the 200 ℃ setting, CPC measurements show extremely low particle counts, indicating insufficient decomposition of $Ni(CO)_4$. This gas has an extremely high toxicity, with a median lethal dose of 3 ppm [56]. Due to this serious safety concern for bulk production of product at lower temperatures, further experimentation into this range is discontinued. A homogeneous coating could potentially be obtained by delving into lower temperatures, but it would likely involve incomplete decomposition of all nickel tetracarbonyl gas.

This inability to form a conformal layer could be attributed to the generally poor wetting nature of molten Ni due to its high surface tension relative to other metals. The wettability of molten nickel on a solid bare aluminum surface has not been specifically investigated, however, since aluminum surface experimentation generally involves an aluminum oxide layer. My experiment presents an opportunity to have rapidly cooling molten nickel on a solid aluminum particle because the $Ni(CO)_4$ decomposition temperature is below the aluminum melting point. The results suggest that Ni does show poor wettability for this case, and indicates moving to a different metal coating could promote formation of a conformal layer.

3.4 Conclusions

A method is presented for aerosol production of a heterogeneous decoration of nickel particles on the surface of in-situ generated nanoaluminum. A slow air bleed to passivate the product is shown by XPS to oxidize a majority of this nickel to form Ni_2O_3, and further XPS evaluation shows formation of a thicker aluminum oxide than in uncoated

samples; an outcome attributed to heating during nickel oxidation increasing the diffusivity of oxygen into the aluminum core.

Combustion cell tests show poor reactivity for this product in thermite combination with CuO. The highest reactive response is shown with a stoichiometric amount of CuO added considering complete contribution of Ni_2O_3 as an oxidizer. This result, however, shows a significant decrease in pressure rise and prolongation of burn time compared to the uncoated case. Reduced ignition temperatures for the coated case indicate a nickel oxide coating could yield a valuable product if a thinner coating layer does not hinder energy release.

Further experimentation to obtain a homogeneous coating layer of nickel oxide by lowering decomposition temperature of nickel tetracarbonyl is terminated due to high toxicity safety concerns with incomplete decomposition. Based on these results, however, it is worth exploring if a different type of metal oxide coating produced with a lower furnace temperature to avoid a rapid quench will promote homogeneous nucleation, give practical combustion pressure response, and show a similar effect on ignition temperature.

Chapter 4: Fe_3O_4 Coating of Aluminum

4.1 Literature Review

Production of a thin layer coating of Ni/Ni_2O_3 proved unsuccessful, but other metals/metal oxides could potentially yield a homogeneous coating to alter reaction mechanisms. As discussed previously, iron coatings on aluminum particles have resulted in decreased agglomeration during combustion, increasing their efficiency [16]. Similar coatings have shown decreased critical ignition temperature attributed to alloying between aluminum and iron [18]. Since iron is highly reactive, it is likely that a thin coating layer will oxidize completely during an air bleed. Such an iron oxide coating could still improve energetic properties by the exothermic alloying reaction detailed previously [20] or by performing as a directly delivered oxidizer.

In order to develop a coating of iron oxide on the aluminum particles to explore its potential to passivate and functionalize the surface, an appropriate iron production method had to be selected. A subsequent air/argon bleed after coating will allow the iron to react to form the oxide. Current techniques for iron via chemical methods in solution include microemulsions [57], chemical coprecipitation [58], liquid phase reduction [59], and electrodeposition [60]. These batch methods, though dependable, are not easily incorporated to an aerosol system for continuous flow.

Gas phase reduction can be accomplished by heat reducing iron ores such as goethite or hematite with hydrogen gas [61], but a simpler gas phase process has been shown via decomposition of iron pentacarbonyl and subsequent chemical vapor condensation of iron [62,63]. Such CVC experiments have shown thermal pyrolysis of iron pentacarbonyl at relatively low temperatures to form iron particles and gaseous byproduct

CO. The inherent aerosol process lends itself to coupling with the aluminum scheme for a coating, avoiding safety and scale-up concerns with batch processing of unpassivated aluminum for a coating technique. These details combined with previous experience with the technology led to its selection for iron production.

4.2 Experimental Setup

4.2.1 Fe_3O_4 Coated Aluminum Synthesis

The basic experimental configuration is shown in Figure 4.1. The bare aluminum production technique detailed in Chapter 2 involves bubbling of argon through 60 °C heated triisobutylaluminum precursor with a partial pressure of 3.3 mmHg and subsequent thermal pyrolysis at 350 °C in a total flow of 3000 sccm. This aerosol system was coupled with the adapted chemical vapor condensation experiment for thermal decomposition of iron pentacarbonyl.

The final iron production setup consisted of a glass bubbler filled with 25 mL of $Fe(CO)_5$ through which flow-metered argon is passed at a rate of 50 sccm. Due to the high vapor pressure of the liquid at room temperature, it was not necessary to heat the precursor, resulting in a $Fe(CO)_5$ partial pressure of 28.3 mmHg in argon. This product is combined with the aluminum nanoparticle aerosol consisting of an aluminum total mass flow of $1.3 \cdot 10^{-2}$ g/min, and passed to a 15.5 inch tube furnace with a residence time of 1.8 seconds at 175 °C to decompose the iron precursor and minimize any alloying reactions with the aluminum.

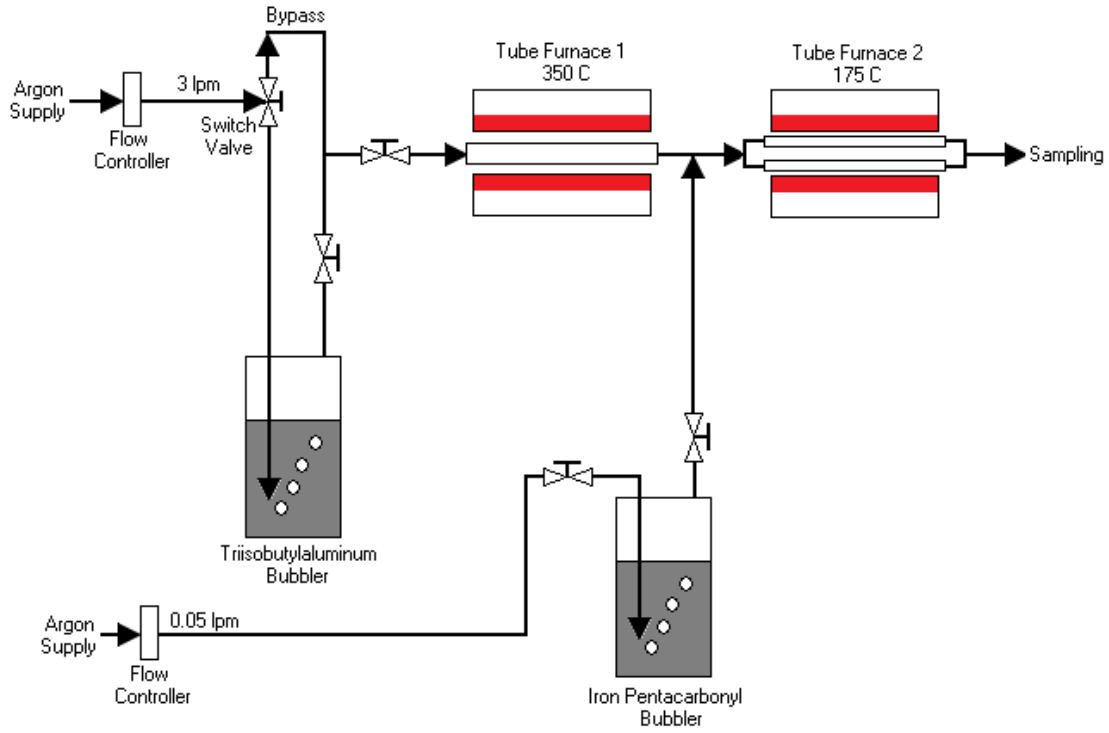

Figure 4.1: Experimental setup for iron oxide coating of aluminum via pyrolysis of iron pentacarbonyl.

Due to concerns with iron pentacarbonyl toxicity, all downstream lines were completely flushed with argon after collection of the product. Addition of multiple three way Swagelok valves and purge lines allow for proper ventilation, but are not shown in Figure 4.1. Due to the pyrophoric nature of the iron coating, following collection of the material a slow bleed of a lean air/argon mix is sent through the product while heating the holder to 50 °C with heating tapes to allow for passivation of product to yield the iron oxide coating.

4.2.2 Product Evaluation Apparatus

– SMPS, HRTEM/EDS, XPS, Pressure Cell Combustion: detailed in Section 2.2.2

– Wire Temperature Jump Ignition and High Speed Video: detailed in Section 3.2.2

4.3 Results and Discussion

4.3.1 Product Inspection

Final conditions for iron oxide coating employed a decomposition furnace temperature of 175 °C with an outlet flow of $4.3 \cdot 10^{-3}$ g/min Fe for 100% theoretical precursor conversion combined with the aluminum aerosol mass flow of $1.3 \cdot 10^{-2}$ g/min, resulting in a 0.33 value for Fe/Al mass ratio. The Fe/Al mass ratio corresponds to a theoretical iron oxide coating of 6.4 nm on an 87 nm Al particle for 100% condensation of iron onto the particle surface. The low vapor concentration of iron should promote homogeneous condensation over heterogeneous nucleation.

Obtaining a coating thickness based on experimental production of iron requires knowledge of the particle size distributions for both the aluminum and the iron material. These are acquired separately using the scanning mobility particle sizer system composed of a differential mobility analyzer coupled with a condensation particle counter, an experimental system detailed previously.

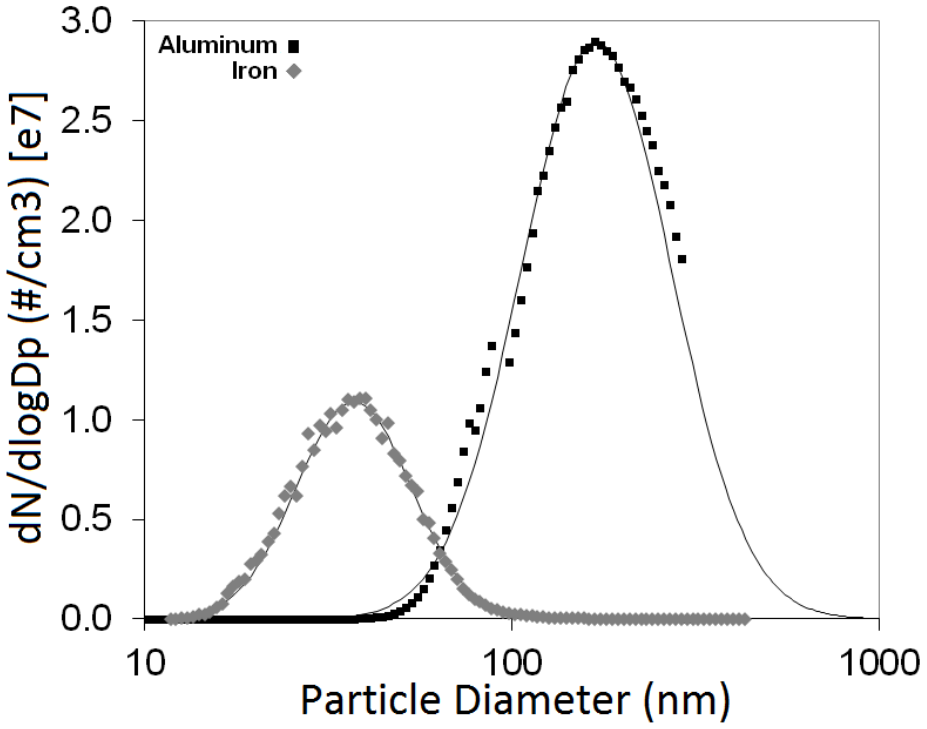

Figure 4.2: Experimental and lognormal fitted particle size distributions for iron and aluminum, measured separately.

SMPS size measurements are fit to lognormal distributions for the plots in Figure 4.2. Pure iron particle measurements are converted into an iron oxide basis, and iron oxide thickness can be determined. The mass ratio of Al to Fe based on these experimental results gives a value of 0.29, resulting in a coating thickness of 5.75 nm Fe_3O_4. The slight difference between the theoretical coating thickness and calculations based on experimental size distributions can be attributed deposition of iron pentacarbonyl precursor to the tube walls.

Product collected from the iron coating system was passivated with air to form iron oxide, and once a stable sample was obtained it was examined using the high resolution TEM. Examples of coated product particle imaging are shown in Figure 4.3. The TEM shows a ~5 nm amorphous conformal coating on the aluminum particle.

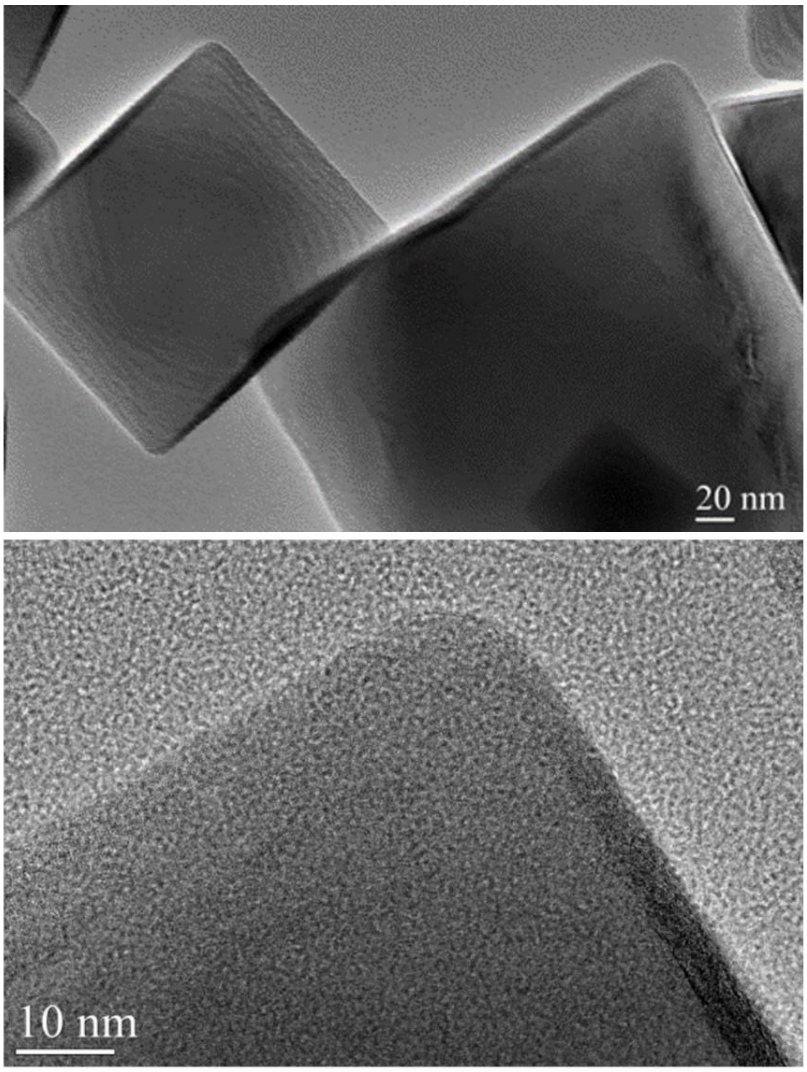

Figure 4.3: High resolution TEM images of polyhedral particles from the iron oxide coating experiment.

To determine the chemical nature of the coating, energy dispersive X-ray spectroscopy characterization was performed, and the results shown in Figure 4.4 clearly indicate that the shell on the aluminum does in fact contain iron and oxygen. Since high resolution imaging showed the shell to be amorphous, it is likely that the iron coating has oxidized completely during the air bleed to form a homogenous iron oxide coating. Due to minor image shifting during measurements, EDS line scan plots cannot be used for direct

quantification of iron oxide coating thickness but only to confirm the presence of iron at the edge of the particle.

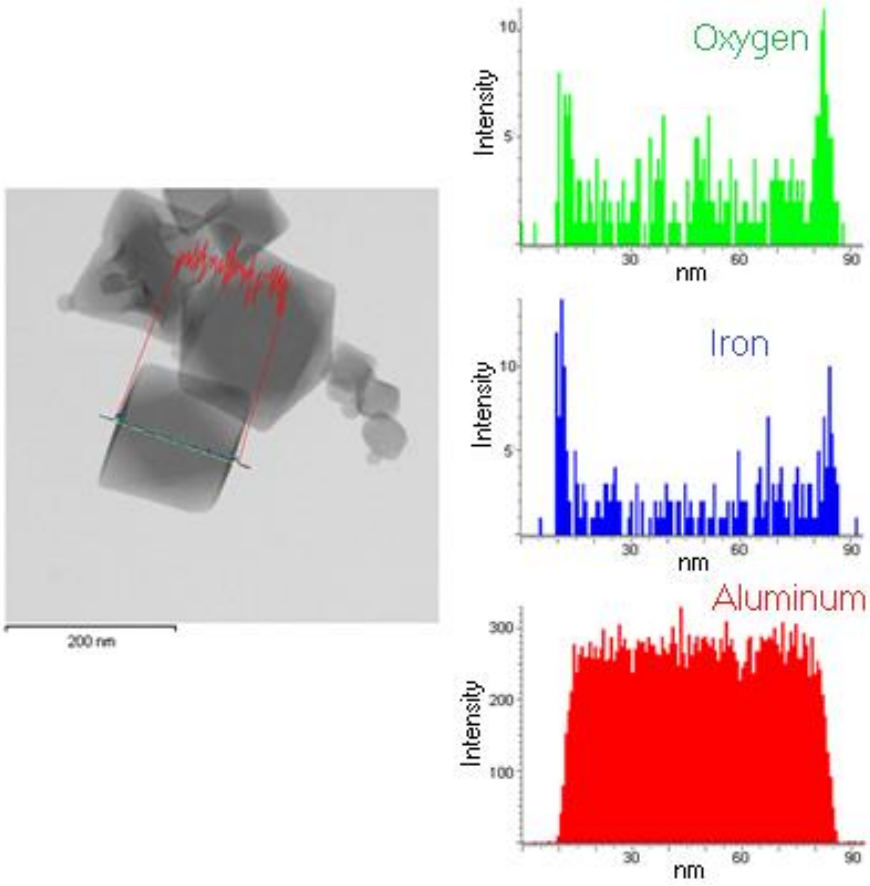

Figure 4.4: EDS linescan of a polyhedral aluminum particle from the iron coating experiment.

The presence of iron, oxygen, and aluminum at the edge of the particle could indicate the development of a mixed metal oxide phase such as $FeAl_2O_4$ hercynite or an amorphous coating of composition proportional to $FeO \cdot Al_2O_3$. As high resolution TEM demonstrates the coating to be completely amorphous, the presence of any crystalline hercynite can be ruled out. To further evaluate the composition of the amorphous layer on the aluminum surface to establish the phase of iron oxide or a potential mixed metal oxide, X-ray photoelectron spectroscopy results for the aluminum and iron phases are shown in

Figure 4.5 and 4.6, respectively. This gives elemental analysis of the top ~10 nm of the particle, with penetration distance depending on the density of the material.

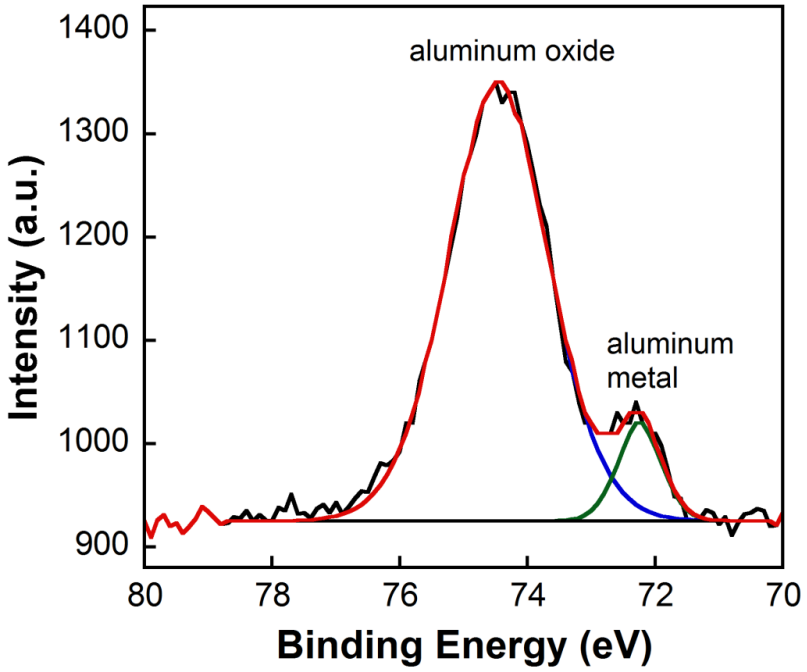

Figure 4.5: XPS Al spectrum for iron oxide coated Al nanoparticles.

Figure 4.5 demonstrates unambiguously that aluminum oxide has formed on the surface of the aluminum core despite the iron oxide coating. It is clear that the iron oxide coating either did not act as passivation layer or the iron oxide itself continuously reacted with the underlying aluminum. The aluminum oxide peak matches well with literature data and no additional peaks are present.

Further analysis of the aluminum and aluminum oxide XPS peaks for this coated material compared to results from untreated aluminum reveals a result similar to that of the Ni/Ni_2O_3 coating in Chapter 3. The relative peak heights in Figure 4.5 for $Al:Al_2O_3$ compared to the previous result for uncoated synthesized Al in Figure 2.6 show a much higher ratio for the uncoated case; indicating the aluminum oxide layer is in fact larger for the iron oxide coated case. Iron oxide coating on the aluminum surface has thus not

passivated to prevent aluminum oxidation; it has facilitated slightly increased aluminum oxidation.

An understanding of metal oxides as an oxygen lending agent makes this result sensible. At high temperatures, iron oxide will release oxygen that can be consumed by the bare aluminum. The iron oxide coating will continue taking up oxygen from the environment and passing it along to aluminum, thus growing an aluminum oxide shell, until this barrier becomes too large for oxygen to diffuse through. The heat released during the oxidation of iron may enable a deeper penetration of oxygen into the aluminum than in an uncoated case. For further examination of the iron oxide material on the surface, XPS results can be analyzed to determine the phase of the iron.

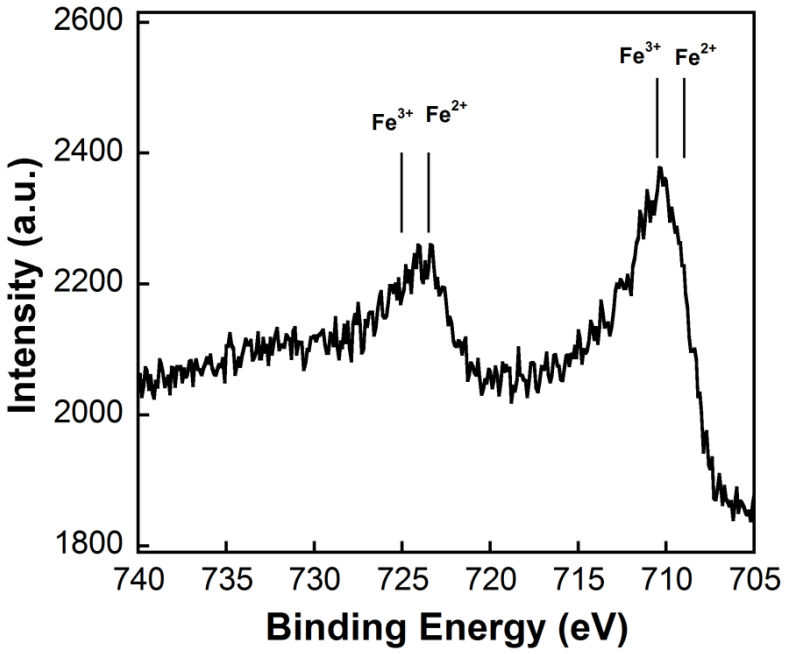

Figure 4.6: XPS results for iron in product particles.

Analysis of Figure 4.6 and comparison to XPS reference tables for iron phases reveals that the material on the particle surface is Fe_3O_4, iron (II, III) oxide [64], which has formed during the low temperature passivation with air. In summary, information from

XPS combined with EDS linescans leads to the conclusion that this is a pure aluminum core with an Al_2O_3 shell surrounded by a Fe_3O_4 layer.

4.3.2 Reactivity Investigation

To examine the energetic properties, bulk product was collected from the iron oxide coating experiment on polypropylene membrane filters. For evaluation of the impact caused by the coating during combustion, the material was combined with a stoichiometric amount of CuO from which a 25 mg sample was ignited and burned in the closed volume combustion cell instrument with pressure and optical sensing. Combustion tests were performed in the cell for uncoated synthesized Al/CuO, Fe_3O_4-coated-Al/CuO, and commercial Al/CuO.

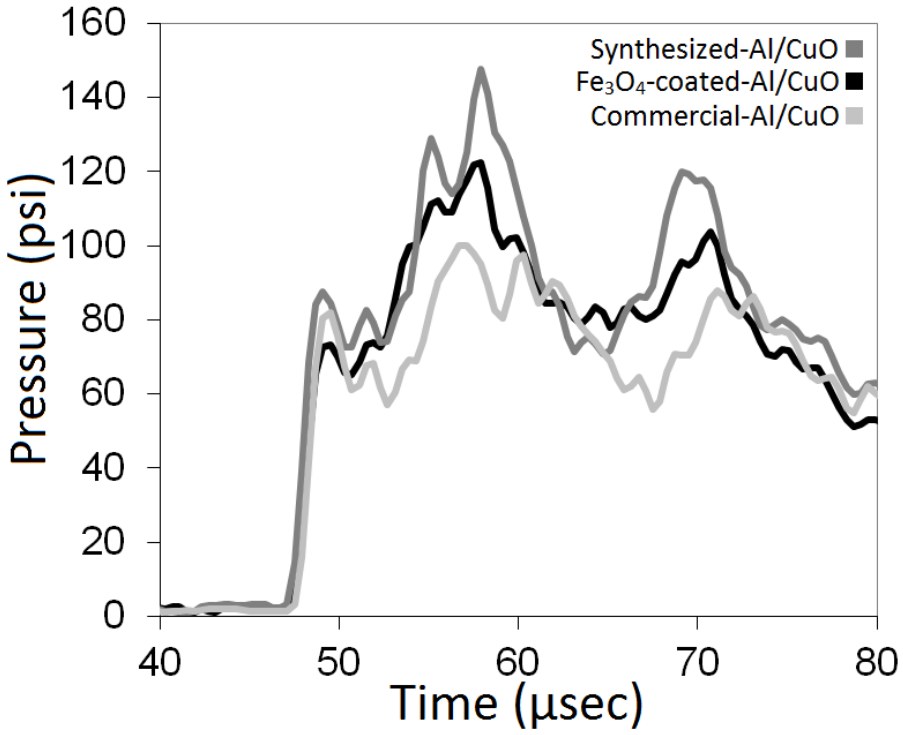

Figure 4.7: Pressure response from combustion tests of Fe_3O_4-coated-Al compared to uncoated synthesized and commercial Al with stoichiometric CuO.

Figure 4.7 shows the temporal pressure response for a CuO based stiochemetric thermite mixture of the uncoated and coated Al particles. The Fe_3O_4-coated-Al/CuO combination shows a very similar trend to the uncoated material with a slightly attenuated response. The maximum pressure values are 122 psi and 148 psi for coated and uncoated, respectively, with similar pressurization rates.

Thus, the coating has not yielded an enhanced reactivity in terms of pressure. This result can be explained by referencing the XPS results for the coated product in Figure 4.5 showing an increased thickness of the aluminum oxide layer. The product has slightly lower fuel content and an increased barrier to reaction. It should be noted, however, that the Fe_3O_4-coated-Al/CuO pressure cell result still shows a pressure response slightly higher than commercial nanoaluminum/CuO, which gives a maximum pressure of 100 psi.

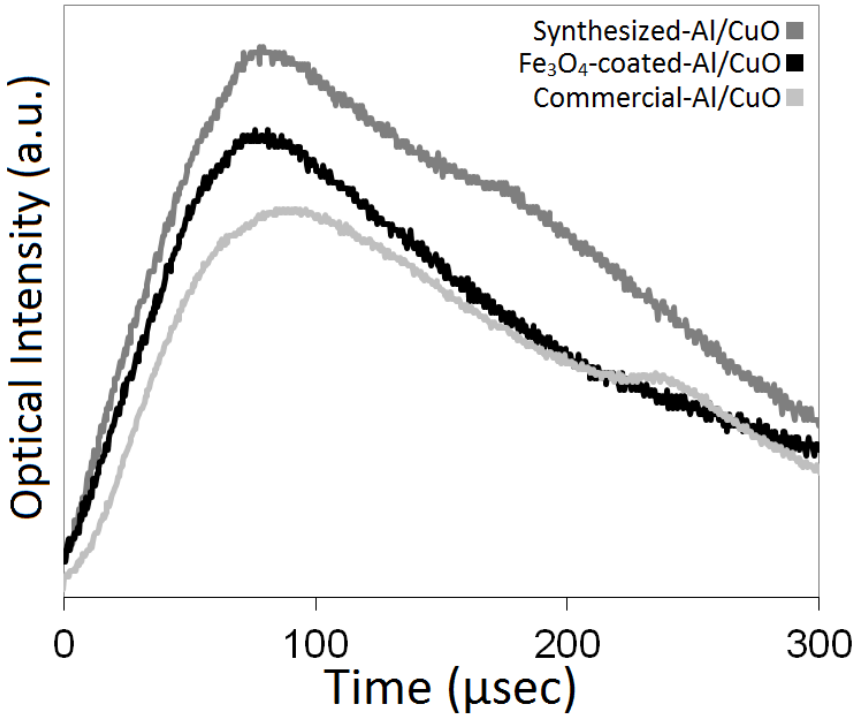

Figure 4.8: Optical response from combustion of Fe_3O_4-coated-Al compared to synthesized and commercial Al with stoichiometric CuO.

Figure 4.8 shows the temporal optical response indicating a FWHM of 182 μsec for Fe_3O_4-coated-Al/CuO, compared to 218 μsec for uncoated synthesized Al/CuO and 224 μsec for commercial nanoaluminum/CuO. This could indicate an enhancement in terms of rate of energy release for the coated material, but examination of the pressurization rates proves this not necessarily the case; a value of 11.8 psi/μsec for the Fe_3O_4-coated-aluminum/CuO compared to 13.7 psi/μsec for the uncoated synthesized Al/CuO and 10.4 for commercial Al/CuO.

Though the iron oxide coated aluminum thermite may burn completely in a shorter total time, the rate at which maximum pressure is accomplished from the start of the event is similar to that of uncoated synthesized aluminum thermite. For comparison, uncoated synthesized aluminum was combined with commercial nanoFe_3O_4 along with stoichiometric CuO with ratios approximated to the amount of Al and Fe_3O_4 present in the coated sample. These ratios were calculated for a theoretical coating of 2 nm iron oxide on top of the aluminum oxide layer on a particle of bipyramidal shape. This material was then tested in the pressure cell, and results are shown in Table II.

The ignition temperatures of these materials were then determined from hot wire T-jump measurements, described previously in Section 2.2.2. Stoichiometric thermite mixtures with CuO were sonicated in hexane and deposited on the thin platinum wire for combustion. Calculated ignition temperatures averaging three runs with a heating pulse of ~3 ms are shown in Table II, along with the pressure cell results.

Table II. Pressure cell results comparing commercial Al, synthesized Al, Fe_3O_4 coated Al, and synthesized Al with nanoFe_3O_4; all combined with stoichiometric CuO.

Sample	Pressure Rise (psi)	Pressurization Rate (psi/μsec)	Burn Time (μsec)	Ignition Temperature (K)
Commercial-Al/CuO	100.1	10.4	224.0	~1040
Synthesized-Al/CuO	147.5	13.7	218.0	~1057
Fe_3O_4-coated-Al/CuO	122.5	11.8	182.0	~973
Synthesized-Al/CuO + added nanoFe_3O_4	142.6	14.3	215.2	~1112

The ignition temperature results for these tests, with each value averaged from three T-Jump runs, allow comparison between samples with precision; all standard deviations are under 20 K. In terms of temperature accuracy, the ultra-high frame rate of the Phantom V12 camera ensures extremely fine time resolution for identifying of the point of ignition. A slight error of +/- 10 K, however, is associated with matching this point to the step-wise temperature plot from the wire resistance measurement. Nonetheless, the precision of our values indicates that a comparison between samples is worthwhile.

T-Jump ignition tests show a decrease in critical ignition temperature for the Fe_3O_4 coated aluminum thermite case; a value of 973 K compared to 1057 K for the uncoated synthesized Al thermite. However, the simple addition of Fe_3O_4 nanoparticles to Al/CuO does not show a decrease in ignition temperature, and thus it is clear that the addition of the iron oxide coat has modified the transport rates of either aluminum of oxygen across the alumina coating. The reduction in ignition temperature is not as drastic as the Ni_2O_3 coated case showing a value of 923 K, but this could partly be attributed the lower mass of coating present for the homogeneous coating.

This is consistent with prior work by Andrzejak *et al.* who showed a decreased ignition temperature for millimeter sized iron-coated aluminum particles caused by the formation of intermetallic Al-Fe alloys during combustion [18]. Since the aluminum particles are coated with iron oxide as opposed to pure iron, however, it cannot be assumed that the two materials follow similar reaction pathways. The route is more likely to be similar to that shown by La *et al.* for formation of Fe_3Al by reaction of iron oxide with aluminum [20], though this case will be altered due to the Fe_3O_4 phase.

4.4 Conclusions

This study presents an aerosol technique for production of an iron coating on bare nanoaluminum via gas phase pyrolysis of iron pentacarbonyl. Subsequent air/argon bleed to passivate iron is shown by XPS to completely oxidize the coating into Fe_3O_4. It was observed that the oxide thickness at interface also included oxidation of aluminum. Added Al_2O_3 thickness is attributed to two causes: the Fe_3O_4 coating acting as a donor, and iron oxidation heating the particle surface to increase the diffusivity of oxygen into the aluminum.

Pressure cell combustion tests with a stoichiometric thermite mixture of Fe_3O_4-coated-Al/CuO show a slightly lower pressure release compared to the uncoated case which is attributed to the enlarged aluminum oxide layer formed during passivation. Temperature jump ignition tests for critical ignition temperature measurement of stoichiometric thermite mixtures reveal a lower value for the Fe_3O_4 coated case. This reduction could indicate an exothermic alloying reaction between aluminum and iron, as has been previously shown for iron coated aluminum in the literature.

Chapter 5: Perfluoropentanoic Acid Coating of Aluminum

5.1 Literature Review

To obtain a successful passivation coating on aluminum, a more worthwhile approach than a physisorbed coating could be to chemisorb material to the aluminum surface. With aluminum atoms at the surface of the particle chemically bound to another material, ambient oxygen cannot react and penetrate to form an alumina shell. Furthermore, if this coating layer is chemically bound to the surface, only a monolayer is required to passivate and any excess unbound material can be removed. If accomplished, passivated product with a monolayer would likely have a very high active aluminum percentage by mass. Taking it a step further, if this chemically bound monolayer can perform as an oxidizer during combustion or otherwise alter the reaction mechanism, the result could prove a novel enhancement for energetic processes.

For an organic passivation coating on aluminum, several options were available. In the nano-regime, the epoxide polymerization technique on aluminum in solution has been demonstrated to be a very successful method for capping and stabilization of aluminum [11]. Though valuable, this method does not translate well to a gas phase coating system due to the multiple step reactions needed to polymerize. Aerosol processes for photoinduced chemical vapor deposition of silica have yielded thickness controlled coatings on different nanoparticles [65], and photoassisted aerosol hydrosilylation with terminal alkenes has been developed for surface modification of silica nanoparticles [66]. Simple techniques with waxes and other organic based materials could also prove fruitful due to their ease of incorporation into a bubbler system. A paraffin wax technique was explored for protection of titanium oxide particles by Balasubramanian *et al.* in a gas phase

evaporation chamber technique [14]. In a similar method, stearic acid was successfully deposited on the surface of silver nanoparticles for protection in an evaporation system by Zhang *et al.* [15]. Information from these bubbler experiments was incorporated into techniques for coating nanoaluminum to allow fine-tuned flow control of coating material, but all of these potential passivation materials would only provide enhancement due to prevention of aluminum oxidation. A coating is desired that not only protects the aluminum core but contributes additional performance characteristics during combustion.

For a functional coating to enhance oxidizer delivery, the use of perfluorocarboxylic acids, though previously accomplished in solution, shows potential for development in an aerosol system [12]. The carboxylic acid group on the end of the fluorocarbon chain should preferentially react with the bare aluminum surface, forming a monolayer for protection from penetration of oxygen. Several perfluorocarboxylic acids were investigated for coating production, but perfluoropentanoic acid ($C_5HF_9O_2$) was ultimately chosen for functionalized passivation as its liquid phase at room temperature and relatively low boiling point of 140 °C allow for ease of incorporation into a bubbler system for gas phase coating.

An aerosol based approach is developed for in-line perfluorocarboxylic acid passivation of synthesized bare nanoaluminum. Aerosol techniques have been heavily studied as valuable continuous production routes for nanoparticle and thin film manufacture, and coating the core material as it is produced avoids potential scale up concerns with passivation processing of batch samples in oxygen-free atmospheres. Under appropriate conditions, gaseous perfluoropentanoic acid (PFPA) treatment of bare nanoaluminum can produce a monolayer that protects the metallic core from thick

aluminum oxide layer formation. This material is then tested for reactivity relative to untreated product, indicating extremely high active fuel content and reduced critical ignition temperature for CuO thermite combinations.

5.2 Experimental Setup

5.2.1 Perfluoropentanoic Acid Coated Nanoaluminum Synthesis

The basic experimental configuration is shown in Figure 5.1. The bare aluminum production technique described previously involves argon bubbled through triisobutylaluminum precursor heated to 60 °C with a partial pressure of 3.3 mmHg and subsequent thermal pyrolysis at 350 °C in a flow of 3000 sccm. This aluminum aerosol, with a total mass flow of $1.3 \cdot 10^{-2}$ g/min Al, is sent to the gas phase coating section employing a glass bubbler containing 25 mL of perfluoropentanoic acid heated to 80 °C with an Omegalux heating tape connected to a variable transformer.

The outlet stream from the bubbler contains the aluminum aerosol flow in a PFPA mass concentration of 10.3 $\mu g/cm^3$ sent through high temperature resistant tubing 20 inches in length heated to 170 °C with a residence time of 1.3 s for collection on Sterlitech 0.2 μm heat resistant polytetrafluoroethylene membrane disc filters. To accomplish a gas phase reaction, the coating zone is heated above the boiling point of PFPA (140 °C) to ensure all coating material remains in the gaseous state. The collection filter is heated to this temperature, as well, to ensure the only acid collected in the product will be the fluorocarbon chains bound to the bare aluminum surface, thus forming a monolayer.

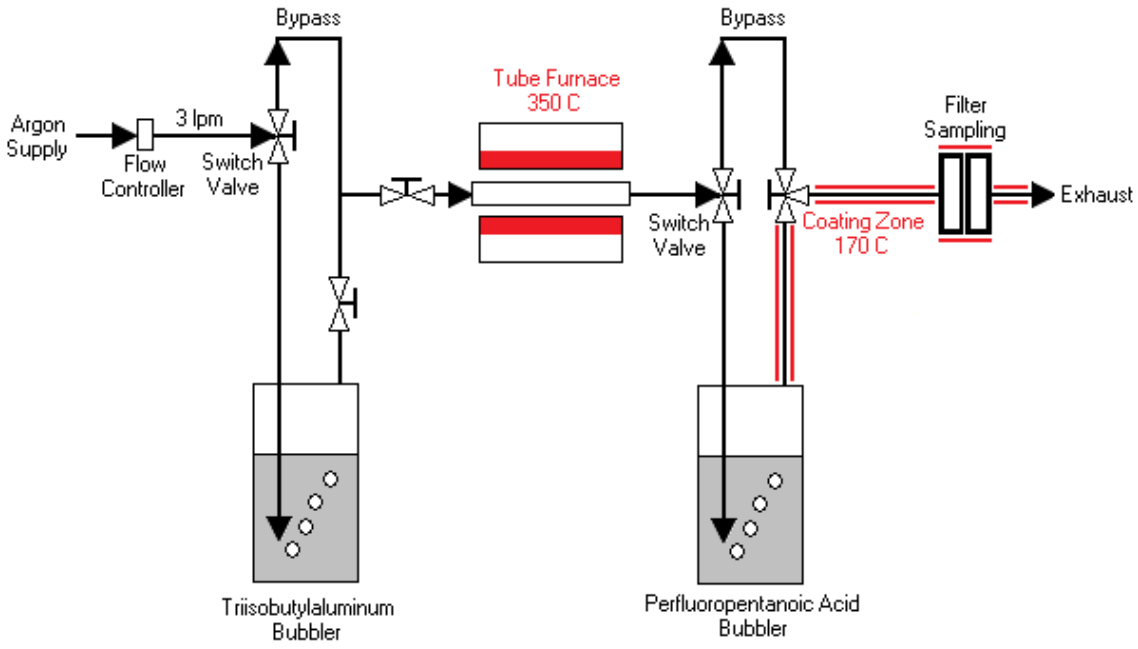

Figure 5.1: Experimental setup for perfluoropentanoic acid coating of Al.

5.2.2 Product Evaluation Apparatus

– SMPS, HRTEM/EDS, XPS Pressure Cell Combustion: detailed in Section 2.2.2

– Wire Temperature Jump Ignition and High Speed Video: detailed in Section 3.2.2

– Fourier Transform Infrared (FTIR) Spectroscopy: infrared spectra were obtained using the Thermo-Nicolet Nexus 670 FTIR utilizing a highly sensitive MCT detector with CaF_2 crystals for sample containment within a nitrogen atmosphere.

5.3 Results and Discussion

5.3.1 Product Inspection

Examination of the high resolution TEM image shown in Figure 5.2a reveals a thin layer coating at the edge of the aluminum particle treated by perfluoropentanoic acid, ranging from 1 to 2 nm; a significant difference from the regular ~4 nm aluminum oxide layer from the untreated case in Figure 5.2b.

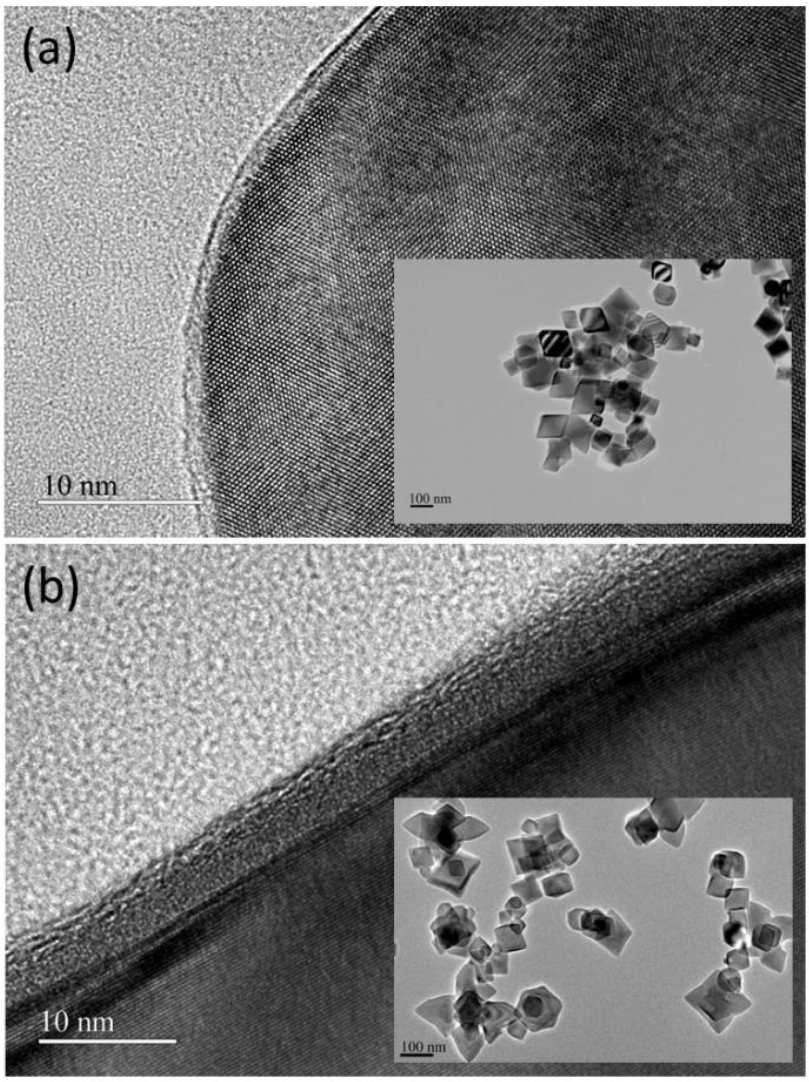

Figure 5.2: High resolution TEM images of nanoaluminum (a) PFPA treated and (b) untreated Note: Insets are lower magnification TEM images of product.

The coated product shows an aluminum core structure identical to previous untreated results yielding single crystalline particles of polyhedral shape, as indicated by the Figure 5.2 insets. The phase of aluminum is confirmed by lattice spacing measurements of 0.229 nm consistent with an accepted value of 0.233 nm.

XPS spectra is then employed to characterize composition of the edge of these particles by analysis of electrons expelled from the top 1 to 10 nm of the particle during irradiation, with penetration distance depending on the density of the material. Results are

fit and shown in Figure 5.3 to analyze the presence of the fluorocarbon in the C1s spectrum for the treated sample, detect the presence of aluminum oxide bonding in Al2p, and compare penetration distance into the metal core for treated and untreated aluminum.

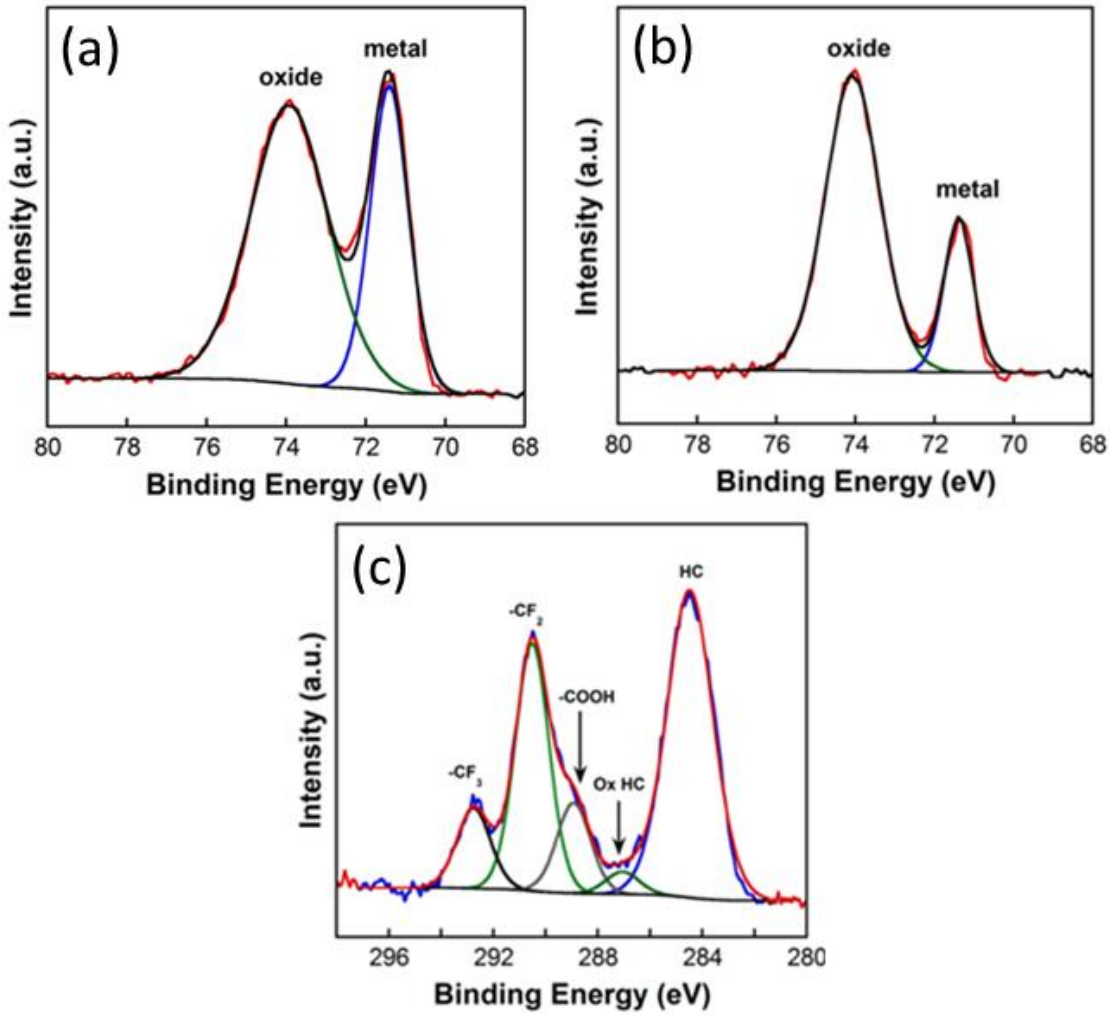

Figure 5.3: XPS spectra for product (a) Al2p PFPA treated (b) Al2p untreated and (c) C1s PFPA treated.

Figure 5.3c demonstrates that fluorocarbon is indeed present at the surface of the particle, indicated by the presence of CF_2, CF_3, and COOH groups. The remaining peaks are attributed to expected hydrocarbon and oxidized hydrocarbon contamination accumulated on the product. Since the collection filter for the coated product is kept above

the boiling point of the PFPA, it can be ensured that all perfluorocarboxylic acid chains are bound to the aluminum surface. To evaluate the aluminum bonding at particle edge, XPS spectra are shown in Figures 5.3a and 5.3b comparing PFPA treated aluminum to untreated, respectively.

Inspection of these results shows a significantly higher aluminum metal peak for the PFPA treated product in relation to the oxide. For the untreated case in Figure 5.3b, the ~4 nm aluminum oxide layer yields an XPS peak with a much higher intensity than that of the pure aluminum metal. Figure 5.3a, however, shows a contrasting result; the aluminum metal peak is higher than that of the oxide. XPS has probed further into the core aluminum than in the untreated case, confirming TEM observations of a significantly thinner coating layer. Additionally, the oxide peak in Figure 5.3a is not entirely attributed to formation of Al_2O_3. In this spectrum, aluminum oxide cannot easily be distinguished from the aluminum bound to oxygen atoms in the carboxylic acid group of the fluorocarbon chain. To analyze the percentage of aluminum oxide formed with relation to functionalized aluminum, the bonding arrangement between the carboxylate groups in the PFPA coating must be analyzed.

There are three potential arrangements for bonding between aluminum and the carboxylic acid group: monodentate coordination involves a single oxygen atom bonding to aluminum while one remains disengaged, bidentate has both oxygen atoms bound to one single aluminum atom, and bridging has each oxygen atom binding to separate aluminum atoms at the surface, as shown in Figure 5.4.

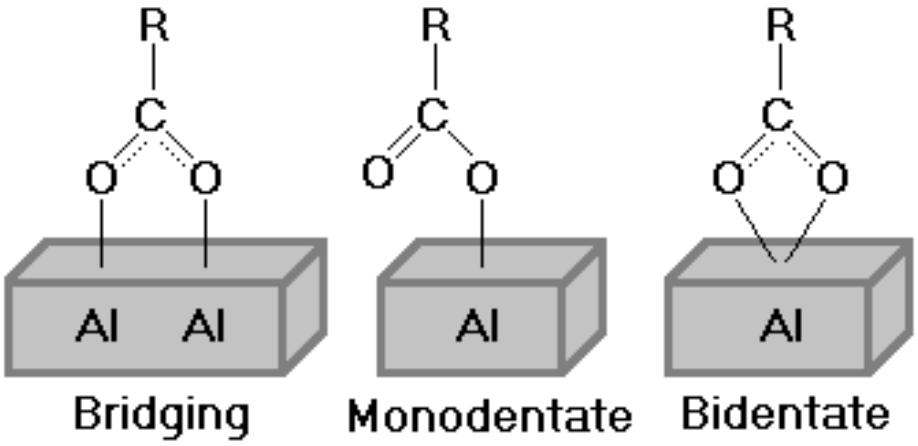

Figure 5.4: Three potential structures for carboxylate binding with the aluminum surface.

Jouet *et al*. found by FTIR examination appropriate frequencies indicating perfluorotetradecanoic acid will adopt the bridging structure [12]. Since the coating layer in this case is composed of a different fluorocarboxylic acid, FTIR spectroscopy is used to investigate if this treatment has formed a similar bonding structure. Resulting transmittance plots are shown in Figure 5.5, and peaks are fitted based on accepted band assignments [67].

Spectra show the change in bonding for the carboxylate group on PFPA. Peaks for ν_a(COO) and ν_s(COO) at 1670 cm^{-1} and 1473 cm^{-1}, respectively, for the treated material in Figure 5.5b give a frequency difference of 197 cm^{-1} fitting with the literature value of ~200 cm^{-1} for the bridging geometry, as was shown by Jouet *et al*. for perfluorotetradecanoic acid [12]. As these peaks are not evident in spectra for untreated aluminum, it can be deduced that the PFPA monolayer on aluminum is bound via carboxylate bridging.

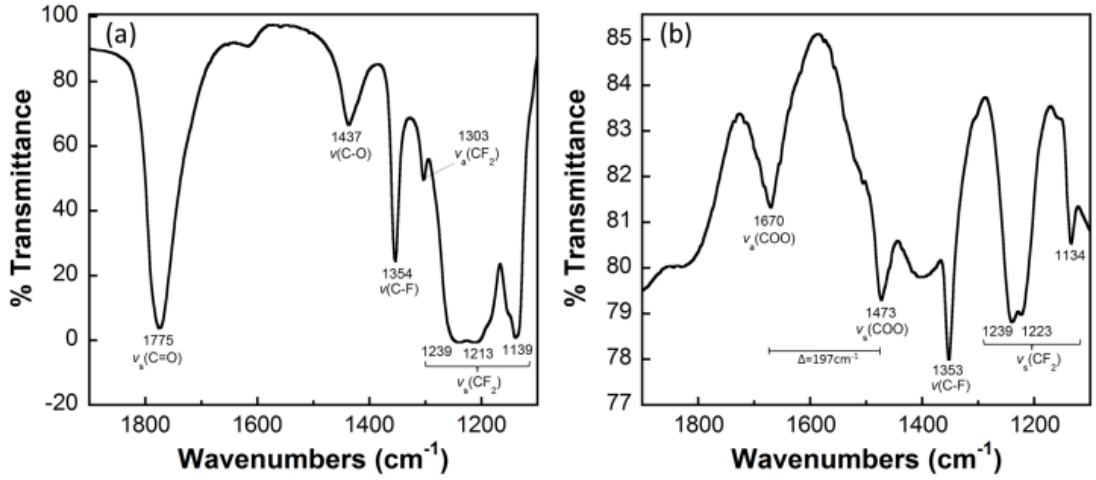

Figure 5.5: FTIR transmittance spectra for (a) free PFPA acid and (b) PFPA coated Al.

Once this coordination is confirmed, peak area percentages for COO^- of 10.5% from the XPS C1s spectrum in Figure 5.3c and a total probe percentage of 29.8% carbon can be multiplied to yield the total percentage of oxygen-Al bonds from carboxylate. A multiplication factor of two is required due to the bridging coordination, resulting in a value of 6.26% total O-Al from carboxylate. Next, an oxide/Al-O-FC peak area percentage of 65.0% from the XPS Al2p spectrum in Figure 5.3a is multiplied by the total probe percentage of 17.1% aluminum to yield the total O-Al bonding percentage of 11.1%. Dividing the O-Al from carboxylate by the total O-Al bonding reveals that 56.3% of the oxide peak is attributed to functionalized aluminum. This calculation assumes that all carboxylate groups are bound to Al since the coating temperature is kept higher than the boiling point of PFPA.

Thus, XPS has shown that not only is the coating layer, seen in TEM Figure 5.2a, much thinner than the untreated case, only 44% of the mass in that 1-2 nm coating is composed of Al_2O_3. In the gas phase bonding between the carboxylic acid group and aluminum, the formation of a small percentage of aluminum oxide indicates that though

the technique has prevented reaction to form a thick oxide layer, there is still a small percentage of available sites. Bridge bonding chains are not fully able to arrange preferentially on the aluminum surface in this gas phase coating system. Since most of the aluminum is successfully bound to carboxylate groups, however, further penetration is successfully averted to avoid significant loss of core material.

The Cabrera-Mott model for oxidation of bare metal nanoparticles details the process to form the alumina layer [68,69]. Initial attachment of oxygen onto the metal surface creates an electric field between the oxide shell and the core, driving diffusion of metal ions outward and coming into contact with oxygen. Results suggest that bonding with the carboxylate group on the fluorocarboxylic acid might alter this electric field and suppress outward diffusion of aluminum ions.

5.3.2 Reactivity Investigation

TGA tests were completed with precise measurement of sample weight gain while heating to 1200 °C, as shown in Figure 5.6. The increase in mass is attributed to complete oxidation of aluminum, and thus results allow for calculation of percentage of active aluminum in the original sample. Weight measurement results show an initial mass of 14.82 mg, a lowpoint mass of 14.04 mg after evaporation of adsorbed water and hydrocarbon contamination, and a final mass of 24.53 mg. The stall in the mass gain between temperatures of 600-700 °C indicates melting of aluminum metal consistent with results shown in Figure 2.10 for untreated aluminum. The difference between the lowpoint and final mass values gives an active aluminum content of 80%, a significant increase compared to the untreated aluminum result of 64% shown previously. This information is consistent with TEM and XPS results showing a much thinner coating layer for the PFPA

treated product. A calculation of theoretical active percentage for an 87 nm particle of bipyramidal shape with coating proportionate to XPS results shows a similar change in active percentage, 65% for uncoated and 83% for PFPA coated aluminum.

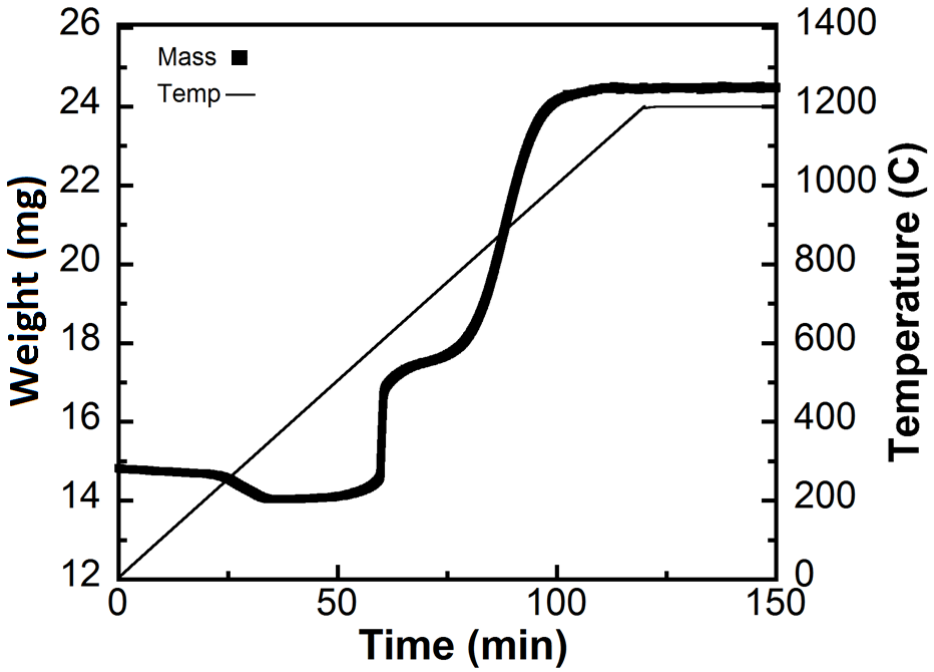

Figure 5.6: TGA experimental data for heating of PFPA treated nanoaluminum.

Since low fuel percentage is one of the major industrial concerns regarding oxide formation, the 16% increase in active aluminum provides strong evidence for gas phase PFPA coating as a practical method for passivation coating. Direct comparison with fuel percentages for commercial nanoaluminum, e.g., Argonide Corp. Al 70% active, avg. diam. ~50 nm [70], can be misleading due to significant variance in content with particle size, but nonetheless a ~90 nm nanoaluminum product at 80% active content can clearly be regarded a valuable result for energetic purposes considering the lower proportions for the untreated samples.

Hot wire ignition testing was accomplished for stoichiometric thermite (sample/CuO) combinations of untreated aluminum, PFPA passivated aluminum, and

aluminum sample allowed to form an oxide layer and subsequently coated with PFPA. High speed video recorded throughout the event allows for visual confirmation of ignition at corresponding time values, as shown in Figure 5.7.

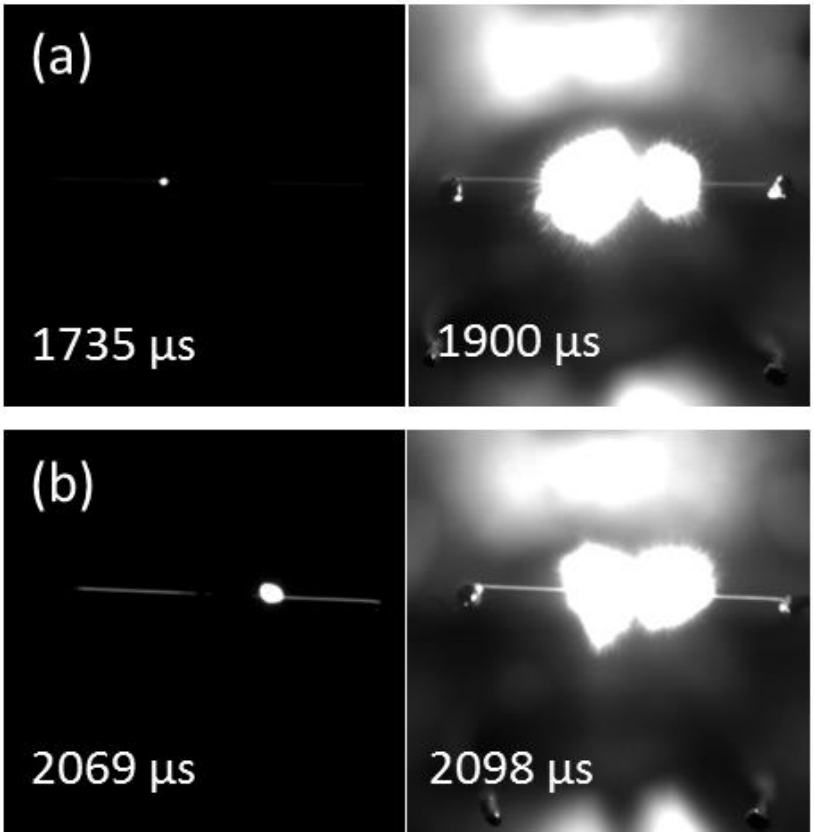

Figure 5.7: High speed video T-jump ignition experiments for (a) PFPA-treated-Al/CuO and (b) untreated-Al/CuO combinations. Note: Same heating rate/pulse in each event.

The coated aluminum in Figure 5.7a shows evidence of ignition considerably earlier than the untreated aluminum, suggesting energetic enhancement. To confirm and calculate critical ignition temperature, appropriate time measurements at the point of ignition are used in conjunction with wire resistance measurements as well as voltage and transient current through the circuit. For further comparison, a sample of aluminum was allowed to form a regular ~4 nm oxide layer and was subsequently coated with PFPA.

Calculated ignition temperatures averaging three runs with a heating pulse of ~3 ms are shown in Table III for the three thermite combinations.

Table III. T-jump Wire Ignition Results Comparing Al, PFPA Passivated Al, and Al (with Oxide Layer) PFPA Coated; All Combined with Stoichiometric CuO.

Sample	Ignition Temperature (K)
Al/CuO	~1057
PFPA-Passivated-Al/CuO	~955
Al(with oxide layer)-PFPA-Coated/CuO	~1003

Results averaged from three runs for each sample show a significantly lower critical ignition temperature of ~955 K for the PFPA passivated Al thermite compared to ~1057 K for the untreated aluminum thermite, both with standard deviations under 15 K. The ignition temperature is also slightly lower for the coated sample with an aluminum oxide layer beneath, indicating a contribution of direct oxidizer delivery via PFPA coating to lowering of ignition temperature. This observation corresponds with results from Pantoya *et al*. detailing an exothermic preignition reaction between aluminum oxide and fluorine to form AlF_3 and exposing the particle core for reaction [25].

Further decrease in ignition temperature for the passivated aluminum sample can be ascribed to the decreased thickness in the aluminum oxide layer. The small amount of Al_2O_3 present can react with fluorine and quickly expose the core to oxidize, whereas a thicker layer will require more time to fluorinate and reveal metallic Al. To probe for fluorinated aluminum in flame ignited passivated sample, XPS is employed to evaluate chemical composition of reaction products, as shown in Figure 5.8.

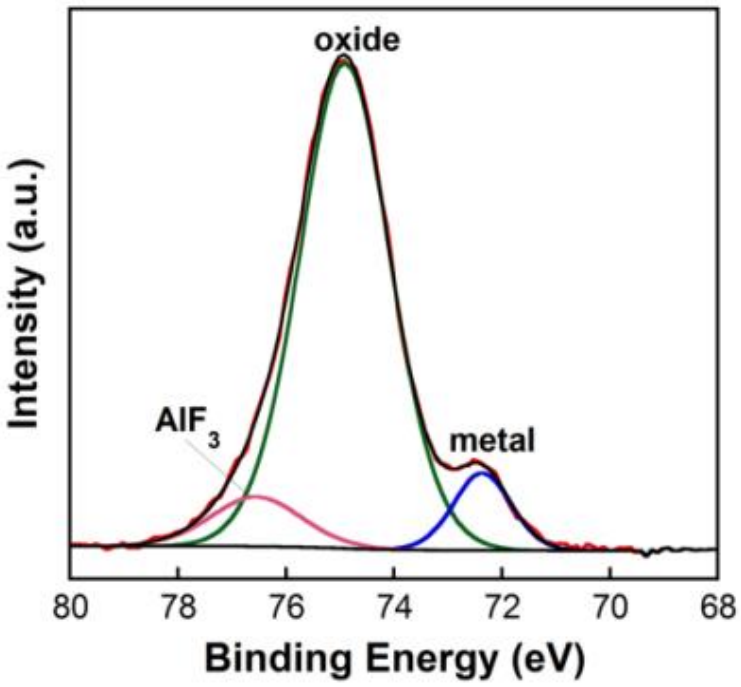

Figure 5.8: XPS Al2p spectrum for flame ignited sample of PFPA treated aluminum.

Formation of AlF_3 in the char product agrees with evidence from thin wire T-jump ignition tests proposing a fluorine-aluminum interaction contributing to decrease in critical ignition temperature. Whether this reaction has occurred between fluorine and core aluminum or substitution with Al_2O_3 by the pre-ignition reaction [25] cannot be determined from these tests.

5.4 Conclusions

A gas phase scheme for coating of bare nanoaluminum with perfluoropentanoic acid is shown by TEM and XPS to protect from penetration of oxygen further than 1 to 2 nm. The coating is indicated by TGA to yield significant improvement in fuel percentage; a value of 80% active aluminum compared to 64% for the untreated case. XPS confirms the presence of the fluorocarboxylic acid, and FTIR analysis determines a bridging carboxylate bonding with the aluminum surface. Hot wire temperature-jump ignition tests

for thermite mixtures with CuO show a decreased critical ignition temperature for the PFPA passivated aluminum thermite compared to untreated. Further testing shows a slight decrease in ignition temperature for oxide passivated aluminum coated with PFPA, indicating contributions from the exothermic reaction for fluorination of aluminum during the combustion event. This theory is upheld by the presence of AlF_3 in XPS spectra for flame ignited PFPA passivated aluminum. Thus, a true functional passivation coating has been produced; a reduced critical ignition temperature is obtained by prevention of thick oxide layer formation and reaction during combustion with the fluorocarboxylic acid layer.

Chapter 6: Summary and Outlook

6.1 Nanoaluminum

Due to the high energy density of aluminum and its rapid energy release when combined with a metal oxide as part of a metastable intermolecular composite (MIC), there is a demand for low cost large scale nanoaluminum processes [1-3]. Current commercial small scale production schemes such as exploding wire and aluminum evaporation from solid pellets have proven reliable, but do not translate well to low cost high yield processes due to their batch production as well as the high amount of energy input required. A simple calculation can show the high cost for large-scale production via the wire explosion process. Construction and particle collection costs should scale similarly between wire explosion and my low temperature aerosol-based approach. Thus the key difference will be the energy input required for wire explosion versus the cost of the triisobutylaluminum precursor. Considering an average kWh market cost, the energy required to explode Al wire at 3000 °C divided by the aluminum yield would scale to $894 per kg of Al produced. If I translate this to the amount of triisobutylaluminum required for a matching Al yield, the cost of precursor would have to be under $122 per kg TibAl, which is within reason for bulk purchase. In addition to this cost of production aspect, focusing on a process for nanoaluminum synthesis that avoids immediate formation of the aluminum oxide layer stimulates subsequent research into coating processes to prevent oxidation to solve this major industrial fabrication issue.

Low temperature gas-phase pyrolysis of triisobutylaluminum was investigated to produce phase pure bare aluminum aerosol nanocrystals. Transmission electron microscopy showed a spherical particle morphology for decomposition of precursor at 500

°C, but lowering furnace temperature to 350 °C allowed for production of primarily polyhedral crystals. Spherical particles were observed to oxidize completely upon a slow air bleed, whereas polyhedral particle samples form a ~4 nm oxide shell during the bleed and remain stable thereafter. Though the bare nanoaluminum in these experiments was passivated with oxygen, the system could easily be coupled with other systems to coat the bare aluminum with other materials for specific energetic applications.

Thermogravimetric analysis of the crystalline product shows an active content similar to commercial nanoaluminum produced by the wire explosion process. Combustion chamber testing reveals a strong increase in energy release for the synthesized sample compared to commercial in thermite combinations with CuO. Considering similar active contents, this clear energetic enhancement is attributed to the highly crystalline nature of the aluminum and its polyhedral morphology altering physical properties during combustion.

Nanoaluminum produced in this capacity can be extremely valuable for use in propellant applications. A fuel that supplies a higher pressure output during combustion can theoretically propel a rocket further for the same amount of fuel mass. Thus, less thermite is required for a particular application, allowing design of smaller fuel compartments and smaller rockets. The bare aluminum aerosol also presented the opportunity to couple with coating systems to passivate and functionalize to yield an even more useful propellant.

Based on these experimental and characterization observations, published in the Journal of Crystal Growth [70], the polyhedral aluminum process developed here shows promise for industrial production and application. As a result, after full assessment an

official US Patent was filed to secure its use, and this application is currently pending review. Following the filing, a company that commercially produces nanoaluminum approached us to evaluate if this process would meet their needs. Though these experiments showed reliable, low cost small scale production by evaporation of precursor, it was clear that industrial processes required alteration to precursor delivery to scale for a large yield.

During collaborations with the Naval Surface Warfare Center at Indian Head, this system modification was explored. Since only a limited amount of precursor can be delivered to the decomposition furnace by evaporation in a bubbler setup, I advised construction of a triisobutylaluminum spraying apparatus to give high aluminum yield. This production system has been built but has yet to be tested using this precursor. Once implemented and tuned, this research has proven that the product will show high reactivity and stability for direct application in the energetics field and help satisfy the high demand for low cost nanoaluminum.

6.2 Ni/Ni_2O_3 Coated Nanoaluminum

As literature suggests, it can prove valuable to coat the bare aluminum aerosol with metals and their oxides. The first approach for coating aluminum to functionalize the surface is with nickel/nickel oxide. Thin layer coatings of nickel have yielded decreased ignition temperatures in experimental studies most likely due to an alloying process also observed in modeling investigations [17,19]. It is worth examining if such a layer would prevent penetration of oxygen into the core upon exposure of the sample, as well.

Nickel tetracarbonyl gas is produced by reaction with CO and subsequently decomposed to deposit nickel on the surface of the in-situ generated bare nanoaluminum

polyhedral crystals. Product inspection with transmission electron microscopy shows a heterogeneous decoration of particles on the aluminum surface, and XPS analysis reveals that the nickel particles have mostly oxidized upon exposure to form Ni_2O_3. Further XPS examination shows that this structural coating will not protect from oxygen penetration, and heat released during oxidation of nickel is likely responsible for furthering formation of a thicker alumina layer. Ensuing combustion chamber testing shows poor response for this product in thermite combination with CuO. Varying combination percentages of CuO in this mixture leads to the conclusion that Ni_2O_3 is likely performing as an oxidizer during combustion, but this direct delivery of oxidizer does not yield energetic enhancement.

As a result, this decorated coating of Ni_2O_3 on nanoaluminum would not be useful in a propellant formulation. Improvement shown by a strong decrease in ignition temperature is outweighed by the poor performance of the material in terms of energy release. The direct oxidizer delivery does not promote rapid energy discharge and an increased alumina layer thickness means a lower active fuel content. Results suggest that a 1-2 nm homogeneous coating of nickel is likely to completely oxidize upon exposure, and this small amount of Ni_2O_3 will be unlikely to further any pressure response or decrease burn time. This heterogeneous coating shows poor results, but if a thin layer homogeneous coated product displays acceptable combustion dynamics, further investigation into a lowered ignition temperature could reveal a useful material. As witnessed by the less drastic decrease in ignition temperature for a thin Fe_3O_4 coating in Chapter 4, however, it could follow that a thinner layer coating of Ni_2O_3 would not result in as radical a reduction.

Due to safety concerns with incomplete thermal decomposition of $Ni(CO)_4$ when delving into lower furnace temperatures, a homogeneous coating was unsuccessful.

Methods with gentler decomposition by photolysis could promote nucleation on the aluminum particle surface. Such a process would likely require a lower concentration of nickel tetracarbonyl and a generous source of photons to ensure complete decomposition of all nickel precursor.

6.3 Fe_3O_4 Coated Nanoaluminum

Based on observations from the first coating approach, I chose to move on to a metal coating process that would allow a lower temperature decomposition of coating precursor. Iron pentacarbonyl vapor does not have such major toxicity issues compared to nickel tetracarbonyl, and this vapor can be thermally cracked at 200 °C [62,63]. Therefore, this technique was a practical choice to promote homogeneous nucleation. Deposition of a layer of this type has been shown to yield a decrease in critical ignition temperature due to an alloying reaction between aluminum and iron [17,19]. As was shown for nickel testing, a thin layer of iron on the particle surface is unlikely to remain in the metallic phase upon exposure to oxygen due to its high reactivity. Even with full formation of iron oxide, however, an alloying reaction could be viable during a combustion event [20]. This evidence combined with the objective to passivate aluminum motivated this investigation.

Liquid iron pentacarbonyl is evaporated via bubbling of argon and decomposed by thermal pyrolysis to grow a coating of iron on the bare aluminum particles. Product is bled with air/argon to oxidize and evaluated by high resolution TEM coupled with EDS, showing a thin homogeneous coating containing iron. XPS assessment shows that this layer did in fact completely oxidize to form Fe_3O_4, and further analysis shows that oxygen has penetrated this layer to form aluminum oxide. An increased thickness of this alumina layer compared to untreated results is again witnessed.

With this type of coating, however, a better understanding of the viability of reactive metals as thin layer passivation coatings is found. As iron is oxidizing on the surface, it passes oxygen inward to oxidize aluminum. Thus it can be concluded that this reactive metal and most likely nickel are not suitable passivating agents on aluminum. A 1-2 nm homogeneous layer will completely oxidize and pass oxygen into the core material. In addition, the local heating from iron oxidation, as was concluded for the nickel coating, increases the diffusivity of oxygen into the aluminum core.

Despite this conclusion in terms of passivation, it was worth continuing experimentation to evaluate if attachment of Fe_3O_4 on the particle surface yielded any enhancements in reactivity. Combustion chamber experiments showed a pressure response only slightly lower than the untreated case, with similar pressurization rates. Thus, this iron oxide coating is not providing an improvement in these tests by direct delivery of oxidizer. Hot wire temperature jump combustion tests, however, reveal significantly lower ignition temperature for the coated material mixed with CuO. This result is attributed to the alloying process similar to that suggested in literature [20].

Since the iron oxide does not passivate or perform well as an oxidizer, this aspect of the coated product does not give any practical use for advancing propellant technology. The coating in this case, however, does not prove to be a significant detriment to combustion. The product still behaves adequately in thermite combinations, so the improvement seen in ignition temperature can be applied as a novel development. The reduction in ignition temperature that is shown through this experimentation can make a valuable difference for a propellant application, allowing ignition to occur closer to the surface of the propellant mixture and permitting design of simpler ignition devices.

Based on experimental results for Fe_3O_4 coated nanoaluminum, currently in press for the Journal of Energetic Materials, further investigation into evaluating this alloying process during the combustion event would be worthwhile. With an understanding of the materials evolved during a fast reaction, it can be selected for more specific applications for best use for this product. For such a thin coating layer, however, combustion of a small sample of thermite powder would likely result in a very small amount of alloyed material. Accordingly, a larger scale evaluation could be necessary.

6.4 Perfluoropentanoic Acid Coated Nanoaluminum

After it became clear that reactive metal coating was not a suitable passivating agent, the approach was altered to select materials that would chemically bind to the bare aluminum in order to keep it from reacting with oxygen. Motivation comes from work by Jouet *et al.* developing monolayers of perfluoropentanoic acid on aluminum in solution to prevent oxide formation [12]. Since acid compounds of this nature contain a large amount of fluorine, they can also help meet goals with direct oxidizer delivery in addition to passivation. This improvement by oxidizer attachment is supported by flame speed studies showing considerable improvement for treated product in cases where the perfluorinated carboxylic acid is attached on top of an aluminum oxide layer [22]. Modification of the coating process to create an aerosol flow for continuous production that will allow for potential scale up to meet industrial demand.

Perfluoropentanoic acid is selected for coating due to its ease of incorporation into the bubbler scheme. The aluminum aerosol stream is passed through this heated PFPA bubbler and passed to a coating zone where the combined aerosol stream is heated above the boiling point of PFPA. The carboxylate group from the acid preferentially reacts with

the bare aluminum, so this high heating ensures production of aluminum with the monolayer without superfluous condensation of PFPA. As a result, a 1-2 nm coating layer is observed and shown to contain the fluorinated compound. XPS spectra shows a deeper probe into the aluminum core, confirming the thinner layer observations from TEM. A bridge bonding coordination between the carboxylic acid and aluminum is evidenced by carboxylate stretching peaks in FTIR, verifying accomplishment of the goal of developing a chemically bound monolayer of PFPA. A small percentage of alumina does form in the product, but the coating successfully prevents penetration further into the core.

Reactivity examinations during high heating with TGA allow for precise measurement of active aluminum content. Results show a substantial increase in fuel content to 80% when the aluminum is treated by PFPA, as was expected based on TEM and XPS observations. The goal of passivating aluminum to prevent significant loss of fuel has been accomplished, saving 16% of the synthesized aluminum that would have been lost without protection, and yielding a product that can give considerable function in propellant applications. This heightened active content means less mass of material is required to pack in a rocket, with less exotic shapes needed to contain fuel compartments.

Combustion of the PFPA treated aluminum in thermite combination with CuO shows a decreased ignition temperature attributed to both the fluorination of aluminum and the decreased oxide layer thickness. This enhancement furthers the practicality of the product, facilitating ignition closer to the surface of the propellant and promoting faster burning of the entire fuel formulation. XPS analysis of flame ignited sample of PFPA treated aluminum shows aluminum will react with fluorine during combustion to form AlF_3, leading to the conclusion that the goal of passivating with a material that can directly

deliver oxidizer has been accomplished; a fuel has been developed that can be ignited easier and propel a rocket further.

These results for gas phase treatment of bare aluminum, submitted for review to Particle & Particle Systems Characterization, open doors to a vast amount of research in both pilot and industrial scale testing. Evidence has been shown for a fluorination reaction encouraging earlier ignition, but further investigations to probe the compounds evolved and consumed during a combustion could give valuable information on the reaction mechanism of the coated material and aluminum as a whole. As this product has a very thin coating with a relatively small amount of fluorine, however, this testing could require larger sample testing to give noteworthy percentages of fluorine containing compounds as they are produced.

Success in passivation and reactivity with this small amount of fluorocarbon encourages future work in longer chain fluorinated carboxylic acids via gas phase reaction. A calculation for the amount of fluorine present in this perfluoropentanoic acid monolayer on a 90 nm aluminum particle of bipyramidal shape shows only enough fluorine to react with 5% of the active aluminum. Since I already see enhanced reactivity based on this small percentage, it would be worthwhile investigating if a higher amount of fluorine delivery would further these results. Since this gas phase reaction method limits coating to a monolayer, however, it would not be possible realistically to deliver enough fluorine to completely consume all available aluminum. A coating layer thicker than a monolayer would be necessary.

Further experimentation can also move on to larger scale testing to easier replicate the environments the fuel would encounter during propellant applications. A high pressure

high density sustained system can completely probe the combustion of these fuels in a fully combined propellant, since this coated aluminum is unlikely to be a stand-alone product. In smaller scale testing of PFPA coated aluminum, combustion in atmospheric pressure systems could allow fluorine to escape and not react. In a high pressure high density system with a fully formulated multi-component propellant, it can be ensured that all fuel and oxidizer will be consumed during a testing event; even if some of the fluorine doesn't react directly with aluminum, it will be utilized as an oxidizer within the formulation. Such large scale research should give further credence to investigations here developing and characterizing a highly active aluminum fuel with a directly bound passivating fluorine compound that demonstrates novel functional qualities to enhance energetic performance.

References

[1] C. Rossi, A. Esteve, P. Vashishta, *Nanoscale energetic materials*. J. Phys. Chem. Sol. **2010**, 71, 57-58.

[2] C. Rossi, K. Zhang, D. Esteve, P. Alphonse, P. Tailhades, C. Vahlas, *Nanoenergetic materials for MEMS: a review*. J. Microelectromech. Sys. **2007**, 16, 919-931.

[3] D. G. Piercey, T. M. Klapötke, *Nanoscale Aluminum – Metal Oxide (Thermite) Reactions for Application in Energetic Materials*. Cen. Eur. J. Energ. Mat. **2010**, 7, 114-129.

[4] S. H. Fischer, M. C. Grubelich, *A Survey of Combustible Metals, Thermites and Intermetallics for Pyrotechnic Applications*, Proc. 32nd AIAA/ASME/SAE/ASEE Joint Propulsion Conference, **1996**, Lake Buena Vista, FL.

[5] T. N. Hall, J. R. Holden, *Navy Explosives Handbook*, NSWCMP **1988**, 88.

[6] R. A. Yetter, G. A. Risha, S. F. Son, *Metal Particle Combustion and Technology*. Proc. Combust. Inst. **2009**, 32, 1819-1838.

[7] E. L. Dreizin, *Metal-based reactive nanomaterials*. Prog. Energy Combust. Sci. **2009**, 35, 141-167.

[8] D. S. Wen, *Nanofuel as a potential secondary energy carrier*. Energy Environ. Sci. **2010**, 3, 591-600.

[9] A. Rai, K. Park, L. Zhou, M. R. Zachariah, *Understanding the mechanism of aluminium nanoparticle oxidation*. Combust. Theor. Model **2006**, 10, 843-859.

[10] G. Jian, N. W. Piekel, M. R. Zachariah, *Time-Resolved Mass Spectrometry of Nano-Al and Nano-Al/CuO Thermite Under Rapid Heating: A Mechanistic Study*. J. Phys. Chem. C **2012**, 116, 26881-26887.

[11] D. W. Hammerstroem, M. A. Burgers, S. W. Chung, E. A. Guliants, C. E. Bunker, K. M. Wentz, S. E. Hayes, S. W. Buckner, P. A. Jelliss, *Aluminum Nanoparticles Capped by Polymerization of Alkyl-Substituted Epoxides: Ratio-Dependent Stability and Particle Size.* Inorg. Chem. **2011**, 50, 5054-5059.

[12] R. J. Jouet, A. D. Warren, D. M. Rosenberg, V. J. Bellitto, K. Park, M. R. Zachariah, *Surface Passivation of Bare Aluminum Nanoparticles Using Perfluoroalkyl Carboxylic Acids*. Chem. Mater. **2005**, 17, 2987-2996.

[13] R. J. Jouet, J. R. Carney, R. H. Granholm, H. W. Sandusky, A. D. Warren, *Preparation and reactivity analysis of novel perfluoroalkyl coated aluminium nanocomposites*. Mat. Sci. Tech. **2006**, 22, 422-429.

[14] B. Balasubramanian, K. L. Kraemer, N. A. Reding, R. Skomski, S. Ducharme, D. J. Sellmyer, *Synthesis of Monodisperse TiO2-Paraffin Core-Shell Nanoparticles for Improved Dielectric Properties*. ACS Nano **2010**, 4, 1893-1900.

[15] L. Zhang, M. B. Ranade, J. W. Genry, *Formation of organic coating on ultrafine silver particles using a gas-phase process.* J. Aeros. Sci. **2003**, 35, 457-471.

[16] A. L. Breiter, V. M. Mal'tsev, E. I. Popov, *Means of modifying metallic fuel in condensed systems*. Comb. Explos. Shock Waves **1988**, 26, 86-92.

[17] E. Shafirovich, P. E. Bocanegra, C. Chauveau, I. Gokalp, U. Goldshleger, V. Rosenband, A. Gany, *Ignition of single nickel-coated aluminum particles.* Proc. of Comb. Inst. **2005**, 30, 2055-2062.

[18] T. A. Andrzejak, E. Shafirovich, A. Varma, *Ignition of Iron-Coated and Nickel-Coated Aluminum Particles Under Normal- and Reduced-Gravity Conditions*. J. Prop. Power **2008**, 24, 805-813.

[19] B. Henz, T. Hawa, M. R. Zachariah, *Molecular Dynamics Simulation of the Kinetic Reaction between Ni and Al Nanoparticles*. J. Appl. Phys. **2009**, 105, 124310.

[20] P. La, J. Yang, D. J. H. Cockayne, W. Liu, Q. Xue, Y. Li, *Bulk Nanocrystalline Fe3Al-Based Material Prepared by Aluminothermic Reaction*. Adv. Mat. **2006**, 18, 733-737.

[21] J. M. Horn, J. Lightstone, J. Carney, J. Jouet, *Preparation and characterization of functionalized aluminum nanoparticles.* AIP Conf. Proc. **2012**, 1426, 607-610.

[22] K. S. Kappagantula, C. Farley, M. L. Pantoya, J. Horn, *Tuning Energetic Material Reactivity Using Surface Functionalization of Aluminum Fuels*. J. Phys. Chem. C **2012**, 116, 24469-24475.

[23] C. A. Crouse, C. J. Pierce, J. E. Spowart, *Synthesis and reactivity of aluminized fluorinated acrylic (AlFA) nanocomposites*. Comb. Flame **2012**, 159, 3199-3207.

[24] K. W. Watson, M. L. Pantoya, V. I. Levitas, *Fast reactions with nano- and micrometer aluminum: A study on oxidation versus fluorination*. Comb. Flame **2008**, 155, 619-634.

[25] M. L. Pantoya, S. W. Dean, *The influence of alumina passivation on nano-Al/Teflon reactions*. Thermoch. Acta **2009**, 493, 109-110.

[26] S. F. Friedlander, *Smoke, Dust, and Haze*. 2 ed. **2000**, New York, NY: Oxford University Press, Inc.

[27] TSI Inc. Model 380-Series Electrostatic Classifier P/N 1930097 Rev. A. **2001**.

[28] K. Park, D. Lee, A. Rai, D. Mukherjee, M. R. Zachariah, *Size-Resolved Kinetic Measurements of Aluminum Nanoparticle Oxidation with Single Particle Mass Spectrometry*. J. Phys. Chem. B **2005**, 109, 7290-7299.

[29] T. K. Sindhu, R. Sarathi, S. R. Chakravarthy, *Generation and characterization of nano aluminium powder obtained through wire explosion process*. Bull. Mat. Sci. **2007**, 30, 187-195.

[30] Y. S. Kwon, Y. H. Jung, N. A. Yavorovsky, A. P. Illyn, J. S. Kim, *Ultra-Fine Powder By Wire Explosion Method*. Scripta Materialia **2001**, 44, 2247.-2251

[31] V. Ivanov, Y. A. Kotov, O. H. Samatov, R. Bohme, H. U. Karow, G. Schumacher, *Synthesis and Dynamic Compaction of Ceramic Powders By Techniques Based On Electric Pulsed Power*. Nanostr. Mat. **1995**, 6, 287-290.

[32] R. Sarathi, T. K. Sindhu, S. R. Chakravarthy, *Impact of binary gas on nano-aluminium particle formation through wire explosion process*. Mat. Lett. **2007**, 61, 1823-1826.

[33] T. K. Sindhu, R. Sarathi, S. R. Chakravarthy, *Understanding nanoparticle formation by a wire explosion process through experimental and modelling studies*. Nanotech. **2008**, 19, 1-11.

[34] I. E. Anderson, J. C. Foley, *Determining the role of surfaces and interfaces in the powder metallurgy processing of aluminum alloy powders*. Surface Interf. Analysis **2001**, 31, 599-608.

[35] J. A. Haber, W. E. Buhro, *Kinetic Instability of Nanocrystalline Aluminum Prepared by Chemical Synthesis; Facile Room-Temperature Grain Growth*. J. Amer. Chem. Soc. **1998**, 120, 10847-10855.

[36] M. Cokoja, H. Parala, M. Schroter, A. Birkner, M. W. E. van der Berg, W. Grunert, R. A. Fischer, *Nanometallurgy of Colloidal Aluminides: Soft Chemical Synthesis of CuAl2 and α/β-CuAl Colloids by Co-Hydrogenolysis of (AlCp*)4 with [CpCu(PMe3)]*. Chem. Mat. **2006**, 18, 1634-1642.

[37] K. A. S. Fernando, M. J. Smith, B. A. Harruff, W. K. Lewis, E. A. Guliants, C. E. Bunker, *Sonochemically Assisted Thermal Decomposition of Alane N,N-Dimethylethylamine with Titanium (IV) Isopropoxide in the Presence of Oleic Acid to Yield Air-Stable and Size-Selective Aluminum Core-Shell Nanoparticles*. J. Phys. Chem. Lett. C **2009**, 113, 500-503.

[38] B. E. Bent, R. G. Nuzzo, L. H. Dubois, *Surface Organometallic Chemistry in the Chemical Vapor Deposition of Aluminum Films Using Triisobutylaluminum: β-Hydride and β-Alkyl Elimination Reactions of Surface Alkyl Intermediates*. J. Amer. Chem. Soc. **1989**, 111, 1634-1644.

[39] A. W. E. Chan, R. Hoffmann, From chemisorption to mechanism on surfaces: *An exploration of the pyrolysis of triisobutylaluminum in the chemical vapor deposition of aluminum thin films*. J. Vac. Sci. Technol. A **1991**, 9, 1569-1580.

[40] D. A. Mantell, *The role of oxygen in chemical vapor deposition nucleation barriers of triisobutylaluminum on silicon*. J. Vac. Sci. Technol. A **1989**, 7, 630-633.

[41] Triisobutylaluminum: CAS 100-99-2; SC2011; Albemarle Corporation: Baton Rouge, Louisiana **1999**.

[42] K. Sullivan, M. R. Zachariah. *Simultaneous Pressure and Optical Measurements of Nanoaluminum Thermites: Investigating the Reaction Mechanism*. J. Prop. Power **2010**, 26, 467-472.

[43] L. Zhou, N. Piekiel, S. Chowdhury, M. R. Zachariah. *Time-Resolved Mass Spectrometry of the Exothermic Reaction between Nanoaluminum and Metal Oxides: The Role of Oxygen Release*. J. Phys. Chem. C, **2010**, 114, 14269-14275.

[44] W. Gong, H. Li, Z. Zhao, J. Chen. *Ultrafine particles of Fe, Co, and Ni ferromagnetic metals.* J. Appl. Phys. **1991**, 69, 5119-5121.

[45] T. Sakai, N. Tsukahara, H. Tanimoto, K. Ota, H. Murakami, E. Kita, *Magnetic anisotropy of Ni Nano-crystals prepared with gas-deposition method.* Scripta Materialia **2001**, 44, 1359-1363.

[46] J. Tang, E. Verrelli, D. Tsoukalas, *Selective deposition of charged nanoparticles by self-electric focusing effect.* Microelectr. Eng. **2009**, 86, 898-901.

[47] T. Hyeon, *Chemical synthesis of magnetic nanoparticles.* Chem. Comm. **2003**, 8, 927-934.

[48] D. H. Chen, S. H. Wu, *Synthesis of Nickel Nanoparticles in Water-in-Oil Microemulsions.* Chem. Mat. **2000**, 12, 1354-1360.

[49] Y. L. Hou, S. Gao., *Monodisperse nickel nanoparticles prepared from a monosurfactant system and their magnetic properties*. J. Mat. Chem. **2003**, 13, 1510-1512.

[50] C. Estournes, T. Lutz, J. Happich, T. Quaranta, P. Wissler, J.L. Guille., *Nickel nanoparticles in silica gel: preparation and magnetic properties*. J. Magnetism Magnetic Mat. **1997**, 173, 83-92.

[51] Y. Q. He, X. G. Li, M. T. Swihart., *Laser-Driven Aerosol Synthesis of Nickel Nanoparticles.* Chem. Mat. **2005**, 17, 1017-1026.

[52] L. Zhou, A. Rai, N. Piekiel, X. Ma, M. R. Zachariah, *Ion-Mobility Spectrometry of Nickel Nanoparticle Oxidation Kinetics: Application to Energetic Materials*. J. Phys. Chem. C **2008**, 112, 16209-16218.

[53] L. Zhou, N. Piekiel, S. Chowdhury, M. R. Zachariah, *T-Jump/time-of-flight mass spectrometry for time-resolved analysis of energetic materials*. Rapid Comm. Mass Spec. **2009**, 23, 194-202.

[54] G. Abadias, A. Debelle, A. Michel, C. Jaouen, F. Martin, J. Pacaud, *Anisotropic strain-stress state and intermixing in epitaxial Mo(110)/Ni(111) multilayers: An x-ray diffraction study*. J. Appl. Phys. **2010**, 107, 023515.

[55] A. N. Mansour, C. A. Melendres, *Characterization of Ni2O3•6H2O by XPS*. Surf. Sci. Spectra, **1994**, 3, 263.

[56] Board on Environmental Studies and Toxicology, *Acute Exposure Guideline Levels for Selected Airborne Chemicals.* Nat. Acad. Press **2008**, 6, 213.

[57] G. P. Song, J. Bo, R. Guo, *The characterization and property of polystyrene compounding of α-Fe_2O_3 in the nano-scale*. Coll. Polym. Sci. **2004**, 282, 656-660.

[58] D. K. Kim, Y. Zhang, W. Voit, K. V. Rao, J. Kehr, B. Bjelke, M. Muhammed, *Superparamagnetic iron oxide nanoparticles for bio-medical application*. Scripta Materialia **2001**, 44, 1713-1717.

[59] G. N. Glavee, K. J. Klabunde, C. Sorensen, G. C. Hadjipanayis, *Chemistry of borohydride reduction of iron(II) and iron(III) ions in aqueous and nonaqueous media. Formation of nanoscale Fe, FeB and Fe2B powders*. Inorg. Chem. **1995**, 34, 28-35.

[60] H. Natter, M. Schmelzer, M. S. Loffler, C. E. Krill, A. Fitch, R. Hempelmann, *Grain-Growth Kinetics of Nanocrystalline Iron Studied In Situ by Synchrotron Real-Time X-ray Diffraction*. J. Phys. Chem. B **2000**, 104, 2467-2476.

[61] L. Li, M. Fan, R. C. Brown, J. V. Leeuwen, J. Wang, W. Wang, Y. Song, P. Zhang. *Synthesis, Properties, and Environmental Applications of Nanoscale Iron-Based Materials: A Review*. Critical Rev. Envir. Sci. Tech. **2006**, 36, 405-431.

[62] C. J. Choi, X. L. Dong, B. K. Kim. *Characterization of Fe and Co nanoparticles synthesized by chemical vapor condensation*. Scripta Materialia **2001**, 44, 2225-2229.

[63] R. Tepe, T. Jacksier, R. M. Barnes, *Determination of iron and nickel in electronic grade chlorine by sealed inductively coupled plasma atomic emission spectrometry*. J. Analyt. Atom. Spectr. **1998**, 13, 989-994.

[64] A. P. Grosvenor, B. A. Kobe, M. C. Biesinger, N. S. McIntyre, *Investigation of multiplet splitting of Fe 2p XPS spectra and bonding in iron compounds*. Surf. Interf. Analy. **2004**, 36, 1564-1574.

[65] A. M. Boies, S. Calder, P. Agarwal, P. Lei, S. L. Girshick, *Chemical Kinetics of Photoinduced Chemical Vapor Deposition: Silica Coating of Gas-Phase Nanoparticles*. J. Phys. Chem. C **2012**, 116, 104-114.

[66] S. Calder, A. Boies, P. Lei, S. Girshick, J. Roberts, *Photo-Assisted Hydrosilylation of Silicon Nanoparticles: Dependence of Particle Size on Grafting Chemistry*. Chem. Mat. **2011**, 23, 2917-2921.

[67] J. Mihaly, S. Sterkel, H. M. Ortner, L. Kocsis, L. Hajba, E. Furdyga, J. Mink, *FTIR and FT-Raman Spectroscopic Study on Polymer Based High Pressure Digestion Vessels*. Croatica Chem. Acta **2006**, 79, 497-501.

[68] N. Cabrera, N. F. Mott, *Theory of the oxidation of metals*. Rep. Progr. Phys. **1948**, 12, 163-184.

[69] V. P. Zhdanov, B. Kasemo, *Cabrera–Mott kinetics of oxidation of nm-sized metal particles*. Chem. Phys. Lett. **2008**, 452, 285-288.

[70] D. A. Kaplowitz, R. J. Jouet, M. R. Zachariah, *Aerosol synthesis and reactive behavior of faceted aluminum nanocrystals*. J. Crys. Growth **2010**, 312, 3625-3630.

Academic Vitae

D. A. Kaplowitz, G. Jian, K. Gaskell, A. Ponce, P. Shang, M. R. Zachariah, *Aerosol synthesis and reactivity of thin oxide shell aluminum nanoparticles via fluorocarboxylic acid functional coating*. Particle & Particle Sys. Char. Submitted March, **2013**.

D. A. Kaplowitz, G. Jian, K. Gaskell, R. Jacob, M. R. Zachariah, *Synthesis and Reactive Properties of Iron Oxide Coated Nanoaluminum*. J. Energ. Mat. In press **2013**.

D. A. Kaplowitz, R. J. Jouet, M. R. Zachariah, *Synthesis and Coating of Aluminum NanoCrystals*. MRS Proc. **2012**, 1405. DOI: 10.1557/opl.2012.226.

D. A. Kaplowitz, R. J. Jouet, M. R. Zachariah, *Aerosol synthesis and reactive behavior of faceted aluminum nanocrystals*. J. Crys. Growth **2010**, 312, 3625-3630. DOI: 10.1016/j.jcrysgro.2010.09.015.

Poster Presentation: 2011 MRS Fall Meeting & Exhibit. D. A. Kaplowitz, J. Jouet, M. R. Zachariah, *Synthesis and Coating of Aluminum NanoCrystals*. Hynes Convention Center, Boston, MA. November 28, **2011**.

United States Patent Application, *Aerosol Synthesis of Faceted Aluminum Nanocrystals.* Inventor: D. A. Kaplowitz, Co-inventors: J. Jouet, M. R. Zachariah. Jointly owned by University of Maryland and Indian Head Division Naval Surface Warfare Center. Serial No. 13/619,017, filed September 14, **2012**.